

The GAPS Programme at TNG[★]

XXXVI. Measurement of the Rossiter-McLaughlin effect and revising the physical and orbital parameters of the HAT-P-15, HAT-P-17, HAT-P-21, HAT-P-26, HAT-P-29 eccentric planetary systems

L. Mancini^{1,2,3}, M. Esposito⁴, E. Covino⁵, J. Southworth⁶, E. Poretti^{7,8}, G. Andreuzzi^{8,9}, D. Barbato^{10,3}, K. Biazzo⁹, L. Borsato^{11,12}, I. Bruni¹³, M. Damasso³, L. Di Fabrizio⁸, D. F. Evans⁶, V. Granata^{12,11}, A. F. Lanza¹⁴, L. Naponiello^{1,15}, V. Nascimbeni¹¹, M. Pinamonti³, A. Sozzetti³, J. Tregloan-Reed¹⁶, M. Basilicata¹, A. Bignamini¹⁷, A. S. Bonomo³, R. Claudi¹¹, R. Cosentino⁸, S. Desidera¹¹, A. F. M. Fiorenzano⁸, P. Giacobbe³, A. Harutyunyan⁸, Th. Henning², C. Knapic¹⁷, A. Maggio¹⁸, G. Micela¹⁸, E. Molinari¹⁹, I. Pagano¹⁴, M. Pedani⁸, and G. Piotto¹²

(Affiliations can be found after the references)

Received ; accepted

ABSTRACT

Context. The measurement of the spin-orbit alignment of hot Jupiters, with a range of orbital and physical properties, can provide information about the evolution of the orbits of this special class of giant planets.

Aims. We aim to refine the orbital and physical parameters and determine the sky-projected planet orbital obliquity, λ , of five eccentric ($e \cong 0.1 - 0.3$) transiting planetary systems: HAT-P-15, HAT-P-17, HAT-P-21, HAT-P-26, and HAT-P-29, whose parent stars have an effective temperature between $5100 \text{ K} < T_{\text{eff}} < 6200 \text{ K}$. Each of the systems hosts a hot Jupiter, except for HAT-P-26 that hosts a Neptune-mass planet.

Methods. We observed transit events of these planets with the HARPS-N spectrograph, obtaining high-precision radial velocity measurements that allow us to measure the Rossiter-McLaughlin effect for each of the target systems. We used these new HARPS-N spectra and archival data, including those from *Gaia*, to better characterise the stellar atmospheric parameters. The photometric parameters for four of the hot Jupiters were recalculated using 17 new transit light curves, obtained with an array of medium-class telescopes, and data from the TESS space telescope. HATNet time-series photometric data were checked for the signatures of rotation periods of the target stars and their spin axis inclination.

Results. From the analysis of the Rossiter-McLaughlin effect, we derived a sky-projected obliquity of $\lambda = 13^\circ \pm 6^\circ$, $\lambda = -26.3^\circ \pm 6.7^\circ$, $\lambda = -0.7^\circ \pm 12.5^\circ$, $\lambda = -26^\circ \pm 16^\circ$, for HAT-P-15 b, HAT-P-17 b, HAT-P-21 b and HAT-P-29 b, respectively. Based on theoretical considerations, these small values of λ should be of primordial origin, with the possible exception of HAT-P-21. Due to the quality of the data, we were not able to well constrain λ for HAT-P-26 b, although a prograde orbit is favoured ($\lambda = 18^\circ \pm 49^\circ$). The stellar activity of HAT-P-21 indicates a rotation period of 15.88 ± 0.02 days, which allowed us to determine its true misalignment angle $\psi = 25^\circ \pm 16^\circ$. Our new analysis of the physical parameters of the five exoplanetary systems returned values compatible with those existing in the literature. Using TESS and the available transit light curves, we reviewed the orbital ephemeris for the five systems and confirmed that the HAT-P-26 system shows transit timing variations, which may tentatively be attributed to the presence of a third body.

Key words. Extrasolar planets – Stars: late-type, fundamental parameters – Techniques: radial velocities, photometric – Stars: individual: HAT-P-15, HAT-P-17, HAT-P-21, HAT-P-26, HAT-P-29

1. Introduction

In more than 20 years of exciting research, exoplanetary science has given many surprises for viewpoints based on our own Solar system. One major surprise came early in the development of this field: the small orbital distances and sometimes large orbital eccentricities of the first known exoplanets (e.g. Mayor & Queloz 1995; Cochran et al. 1997). Since the two giant planets and the two ice planets of the Solar system are much further from the Sun than the four rocky planets are, we would expect a similar situation for exoplanetary systems. This is because the formation of a giant planet requires a core of solid material to grow above a certain critical size of $\approx 10 M_{\oplus}$ in order to start accreting hydrogen and helium (see, e.g., Raymond & Morbidelli 2022). This

phenomenon happens in proto-planetary disks beyond the *snow line*, where there is a steep increase of the density of solid materials (especially volatile compounds with freezing points more than 100 K) that can aggregate to form protoplanets with large cores, which then become giant gaseous planets.

Furthermore, the orbits of these giant planets should be roughly circular. This is because the effective frictional force, which exists for planets that are orbiting within a massive disk of gas and dust, tend to circularize any orbits, even though they are initially eccentric (see, e.g. Raymond & Morbidelli 2022).

Instead, observational results show there are a lot of giant planets with eccentric orbits and located very close to their stars. These planets, which are known as hot Jupiters, are very easy to detect via transit and radial-velocity (RV) methods, and their origin has been one of the main topics of discussion in planetary science for the last 20 years. They most likely formed at large distances from their star, as did Jupiter in the Solar system, but then, through some physical mechanism, have

[★] Based on observations made with the Italian Telescopio Nazionale Galileo (TNG) operated by the Fundación Galileo Galilei (FGG) of the Istituto Nazionale di Astrofisica (INAF) at the Observatorio del Roque de los Muchachos (La Palma, Canary Islands, Spain).

migrated towards the innermost regions. Different mechanisms have been proposed that are able to shrink the orbit of a giant planet. Among them, the main ones are based on (i) dynamical interactions, through planet-planet scattering (Rasio & Ford 1996; Davies et al. 2014) or the Kozai mechanism (see, e.g., Wu & Murray 2003), and (ii) disc-planet interaction (Lin et al. 1996; Ward 1997).

To determine which of the two theories is the right one, or at least the most efficient, one can examine how several parameters are distributed, like the metallicity of the parent stars (see, e.g., Dawson & Murray-Clay 2013) or the eccentricity and the orientation of the planetary orbits of hot Jupiters (see, e.g., Matsumura et al. 2010). For example, it is expected that scattering encounters among planets should randomize the alignments of the orbital planes. Instead, if the existence of hot Jupiters is to be primarily ascribed to disc-planet interactions, we should see many flat architectures, as this mechanism keeps the planetary orbits coplanar throughout the entire migration process. Numerical simulations support these predictions (e.g., Chatterjee et al. 2008; Marzari & Nelson 2009).

Whenever a giant planet undergoes orbital migration, the responsible mechanism is expected also to affect the eccentricity, e , and/or the angle, ψ , between the planet's orbital axis and its host star's spin. Several authors have dealt with this question based on the available data (e.g., Bonomo et al. 2017; Wang et al. 2021; Rice et al. 2021, 2022), but it is still not clear what the degree of correlation between these two parameters is and how much tidal interactions intervene to complicate the interpretation, as recently pointed out by Albrecht et al. (2022). Therefore, new measurements of the spin-orbit alignments are useful for enlarging the sample of exoplanetary systems in order to perform robust statistical analyses and shed new light on what the real cause of the giant-planet migration process is.

While ψ is, unfortunately, not easy to determine, its sky-projected value, λ , can be easily measured for systems containing transiting hot Jupiters, via the observation of the Rossiter-McLaughlin (RM) effect or from star-spot tracking in consecutive transit light curves. Once λ is known, one can derive the true alignment of the projected rotational velocity of the parent star, $v \sin i$. If its radius is also known, its rotation period can be measured as well.

The long-term observational programme GAPS (Global Architecture of Planetary Systems) utilises the HARPS-N spectrograph, at the 3.5 m Telescopio Nazionale Galileo (TNG), to execute a study of the spin-orbit alignment of a sample of known transiting exoplanetary systems for measuring the RM effect (Covino et al. 2013). We took advantage of the high spectral resolution of HARPS-N for targeting faint stars (up to $V < 14$ mag), for which the RM effect is harder to measure at the required level of accuracy (Esposito et al. 2014, 2017; Mancini et al. 2015, 2018).

Photometric follow-up observations with an array of medium-class telescopes support our programme. The aim is to obtain high-quality light curves of planetary-transit events to refine the whole set of physical and orbital parameters of the planetary systems in our target list. High-quality light curves also allow us to detect possible features of the transit light curve, which can be associated with stellar activity (e.g., Mancini et al. 2017), as well as transit timing variations (TTVs).

In this work, we present new measurements of the RM effect for five exoplanetary systems. They have been selected considering the effective temperature of their parent stars, which have $5100 \text{ K} < T_{\text{eff}} < 6200 \text{ K}$ and the eccentricity of the planetary orbits, which are $0.1 < e < 0.3$. We can divide these systems in

two groups. Each of the stars of the first group hosts a hot Jupiter (HAT-P-15 b, HAT-P-17 b, HAT-P-21 b and HAT-P-29 b), whose orbital eccentricity is larger than zero at 3σ confidence level, as estimated by Bonomo et al. (2017). The second group includes only one system, in which there is a Neptune-mass planet, HAT-P-26 b, whose eccentricity was estimated larger than zero at 2σ confidence level by Hartman et al. (2011). For the planets in the first group, we were able to measure the orbital obliquity, but we do not detected any TTVs. For HAT-P-26, we were not able to deduce a precise value for λ , but we detected a TTV.

The paper is organised as follows. In Sect. 2 we describe the systems that are the subject of this study. Spectroscopic and photometric observations and data reduction procedures are presented in Sect. 3. Sect. 4 is devoted to the light-curve analysis. The results of the analysis of the HATNet time-series photometric data are reported in Sect. 6. An analysis of the stellar parameters, based on archival data, is performed in Sect. 7. The stellar atmospheric properties and activity of the stars, based on HARPS-N data, and the measurements of the spin-orbit alignment angle for each of the systems are presented in Sect. 8. The results of the analysis aimed at refining the physical parameters of the systems are reported in Sect. 9. Finally, Sect. 10 contains the discussion, while the main results of this work are summarised in Sect. 11.

2. Targets properties

In this section we summarize the main properties of the five planetary systems that are the subject of this study. The values of the parameters were taken from the Transiting Extrasolar Planet Catalogue (TEPCat¹) and are also summarised in Tables D.1, D.2, D.3, D.4 and D.5.

2.1. HAT-P-15

Kovács et al. (2010) reported the discovery of HAT-P-15 b, a giant planet ($M_p = 1.946 \pm 0.066 M_{\text{Jup}}$; $R_p = 1.072 \pm 0.043 R_{\text{Jup}}$) on an eccentric orbit ($e = 0.190 \pm 0.019$) of period $P_{\text{orb}} \sim 10.9$ days, transiting a G5 V dwarf star ($V = 12.16$ mag, $M_\star = 1.013 \pm 0.043 M_\odot$, $R_\star = 1.080 \pm 0.039 R_\odot$, $T_{\text{eff}} = 5568 \pm 90$ K).

- Kovács et al. (2010) gathered 24 high-precision RV measurements with the HIRES@KECK I, over the time interval August 2007 to December 2009.
- Knutson et al. (2014) collected seven additional RV data points with HIRES (from August 2010 to September 2012) and found no evidence of long-term RV trends, which might indicate the presence of outer companions.
- Ngo et al. (2015) used NIRC2 on Keck II to acquire K -band adaptive-optic (AO) images of HAT-P-15 in two epochs, finding no bound companions.
- Lucky images, which were taken with the AstraLux Norte at the Calar Alto 2.2 m telescope, show two faint objects at separation of 6.2 and 7.1 arcsec, respectively (Wöllert & Brandner 2015). Further observations will be needed to confirm whether these objects are physically associated with HAT-P-15.
- The *Gaia* EDR3 catalogue (Gaia Collaboration 2016, 2021) also reports two objects at a separation of ~ 7 arcsec with $\Delta g \sim 7$ mag; only one of them has a parallax entry that allows us to exclude it as a physical companion.

¹ TEPCat is available at <http://www.astro.keele.ac.uk/jkt/tepcat/> (Southworth et al. 2011).

- Piskorz et al. (2015) analysed NIRSPEC@Keck K -band spectra of HAT-P-15 and did not find evidence of a close redder stellar companion. Subsequent studies of this system (Bonomo et al. 2017; Stassun et al. 2017) confirmed the original estimates of its main physical parameters as reported by Kovács et al. (2010).

2.2. HAT-P-17

HAT-P-17 b is a giant planet ($M_p = 0.54 \pm 0.02 M_{\text{Jup}}$; $R_p = 1.04 \pm 0.02 R_{\text{Jup}}$) on an eccentric orbit ($e = 0.3417 \pm 0.0036$), with period $P_{\text{orb}} \sim 10.3$ d and hosted by a relatively bright early K V dwarf star ($V = 10.54$ mag, $M_\star = 0.88 \pm 0.04 M_\odot$, $R_\star = 0.84 \pm 0.01 R_\odot$, $T_{\text{eff}} = 5322 \pm 55$ K; Howard et al. 2012).

- In ~ 50 HIRES-RV measurements spanning from October 2007 to August 2013 (Fulton et al. 2013; Knutson et al. 2014), evidence was found for the presence of another long period planetary companion, HAT-P-17 c, with $P_{\text{orb}} \approx 10$ to 36 yr, $m \sin i \approx 3.4 M_{\text{Jup}}$, and $e \approx 0.4$. Fulton et al. (2013) also measured the projected obliquity of planet b, finding $\lambda = 19^{+14}_{-16}$, a value which is consistent with zero.
- Bonomo et al. (2017) reported an additional 25 RV measurements taken with HARPS-N from October 2012 to November 2015. With a combined fit of the HIRES and HARPS-N RV data sets, they put more stringent constraints on the HAT-P-17 c parameters: $P_{\text{orb}} = 3972^{+185}_{-146}$ days; $e = 0.295 \pm 0.021$; $m \sin i = 2.88 \pm 0.10 M_{\text{Jup}}$; $a = 4.67 \pm 0.14$ au.
- K -band AO images, taken with the NIRC2 at Keck II (Fulton et al. 2013; Ngo et al. 2015), ruled out the existence of companions with $\Delta K < 7$ mag for separations beyond 0.7 arcsec (65 au according to the Gaia parallax).
- Wöllert et al. (2015) observed HAT-P-17 with AstraLux Norte in the i' and z' passbands. They found no close companions, and reported 5σ detection limits of $\Delta z' = 3.84, 4.95, 6.29, 7.09$ mag at 0.25, 0.5, 1.0, 2.0 arcsec, respectively.
- Similar detection limits in the K_s band were reported by Adams et al. (2013), who used ARIES at the MMT telescope.
- Piskorz et al. (2015) used high-resolution K -band spectra, taken with NIRSPEC@KECK, to search for blended lines from cool stellar companions. They found that the spectral fit is significantly improved by the presence of a 3900^{+200}_{-300} K companion in the HAT-P-17 system at a maximum separation of 36 au.

2.3. HAT-P-21

The exoplanet HAT-P-21 b was discovered by Bakos et al. (2011) to be a massive hot Jupiter ($M_p = 4.063 \pm 0.161 M_{\text{Jup}}$; $R_p = 1.024 \pm 0.092 R_{\text{Jup}}$) moving on a short-period and eccentric orbit ($P_{\text{orb}} \sim 4.1$ d; $e = 0.228 \pm 0.016$) around a G3 V star ($V = 11.69$ mag, $M_\star = 0.947 \pm 0.042 M_\odot$, $R_\star = 1.105 \pm 0.083 R_\odot$, $T_{\text{eff}} = 5588 \pm 80$ K).

- The values of the main physical and orbital parameters of this system reported in the discovery paper are in a good agreement with those from subsequent studies (Torres et al. 2012; Bonomo et al. 2017; Stassun et al. 2017).
- For this star, 15 high-precision RV measurements were obtained with the HIRES@KECK I (from May 2009 to February 2010). K -band images, obtained with the NIRC2 at Keck II (Ngo et al. 2016), showed no evidence of bound

companions. High-resolution Lucky-Imaging observations made with the AstraLux Norte camera also did not reveal the presence of any companions (Wöllert et al. 2015).

- The Gaia EDR3 catalogue reports no objects close to HAT-P-21 within 10 arcsec.

2.4. HAT-P-26

The discovery of the HAT-P-26 planetary system was announced by Hartman et al. (2011). It consists of a low-density Neptune-mass planet ($M_p = 0.059 \pm 0.007 M_{\text{Jup}}$; $R_p = 0.565^{+0.072}_{-0.032} R_{\text{Jup}}$) transiting a K1 V dwarf star ($V = 11.74$ mag, $M_\star = 0.816 \pm 0.033 M_\odot$, $R_\star = 0.788^{+0.098}_{-0.043} R_\odot$, $T_{\text{eff}} = 5011 \pm 55$ K) with a period of $P_{\text{orb}} \sim 4.23$ d. The orbit of this planet is also eccentric, with $e = 0.124 \pm 0.060$.

- 12 RV measurements were obtained for this star with the HIRES@KECK I between December 2009 and June 2010 (Hartman et al. 2011). A further 11 were obtained between December 2011 and June 2012 (Knutson et al. 2014).
- High-resolution Lucky-Imaging observations performed with the AstraLux Norte camera did not reveal close-in bound companions (Wöllert et al. 2015).
- Indications of TTVs in the system, with an amplitude of 4 min and a periodicity of 270 epochs, were observed by von Essen et al. (2019).
- Much more precise measurements of the physical parameters for this system have not been obtained by other authors (Torres et al. 2012; Mortier et al. 2013; Stassun et al. 2017).
- Detailed studies of the atmosphere of HAT-P-26 b have been conducted via transmission spectroscopy (Stevenson et al. 2016; Wakeford et al. 2017; MacDonald & Madhusudhan 2019).
- The Gaia EDR3 catalogue reports no objects close to HAT-P-26 within 10 arcsec.

2.5. HAT-P-29

The HAT-P-29 planetary system is composed of a hot Jupiter ($M_p = 0.767^{+0.047}_{-0.045} M_{\text{Jup}}$; $R_p = 1.064^{+0.075}_{-0.068} R_{\text{Jup}}$), orbiting an F8 V star ($V = 11.90$ mag, $M_\star = 1.199^{+0.063}_{-0.061} M_\odot$, $R_\star = 1.237^{+0.077}_{-0.071} R_\odot$, $T_{\text{eff}} = 6115 \pm 86$ K) every ~ 5.72 d (Buchhave et al. 2011).

- 8 RV measurements were obtained for this star with the HIRES@KECK I between September and December 2010 (Buchhave et al. 2011). Joining these measurements with four others, which were taken with the same instrument between February and August 2012, Knutson et al. (2014) found a trend in the RV data and, hence, evidence for a companion in this system.
- Wöllert & Brandner (2015) found a stellar source 3.3'' away from HAT-P-29, using the AstraLux Norte camera.
- Ngo et al. (2016) confirmed the latter discovery with NIRC2 and found that this source is consistent with a bound stellar companion.
- With 25 high-precision HARPS-N RVs, Bonomo et al. (2017) did not detect any significant trend that can be consistent with the RV drifts found by Knutson et al. (2014), but they found a significant (5.8σ) small eccentricity ($e \approx 0.1$) for the orbit of HAT-P-29 b.

- The measurement of the orbital period of HAT-P-29 b was recalculated thanks to new transit light curves, finding that it is ≈ 17.6 s longer than the previous measurement. No statistically significant TTVs were found (Wang et al. 2018).
- The Gaia EDR3 catalogue (Gaia Collaboration 2016, 2021) reports a faint ($G = 17.8$ mag) object at a separation of 3.43 arcsec from HAT-P-29. However, the parallax of this object indicates a distance roughly 30 times greater than that of HAT-P-29, excluding the possibility of it being a physical companion.

3. Observations and data reduction

In this section we present new times-series spectroscopic data of HAT-P-15, HAT-P-17, HAT-P-21, HAT-P-26 and HAT-P-29, as well as new photometric follow-up observations with TESS and ground-based telescopes.

3.1. HARPS-N spectroscopic observations

All the spectra analysed in this work were acquired with the High Accuracy Radial velocity Planet Searcher – North (HARPS-N; Cosentino et al. 2012) spectrograph at the Italian Telescopio Nazionale Galileo (TNG). The log of the HARPS-N observations is given in Table 1.

HARPS-N provides high resolution spectra ($R \sim 115000$) spanning almost the entire optical range ($\lambda = 383 - 690$ nm), and was designed to deliver very precise stellar RVs (Cosentino et al. 2014). HARPS-N is equipped with its own Data Reduction Software (DRS) that, in addition to 1-D wavelength-calibrated spectra, provides RVs, which are calculated by cross-correlating the spectra with a numerical mask (Baranne et al. 1996; Pepe et al. 2002; Lovis & Pepe 2007) and line bisectors. The DRS also measures the Mount Wilson S index and, if the stellar $B - V$ colour index is lower than 1.2, also the $\log(R'_{\text{HK}})$ chromospheric activity index (Lovis et al. 2011). Specifically, we utilised the latest version of the DRS available offline at the Italian center for Astronomical Archives (IA2) (Smareglia et al. 2014).

HAT-P-15 was observed on the night of 2015/11/16, during a planetary transit. A time series of 33 spectra covered the 5.5 hours long transit from 0.9 hours before ingress to 1.8 hours after egress (see Table 1). With an exposure time of 900 s, the spectra have an average signal-to-noise ratio of 30 (S/N per pixel in 1-D spectra at 5500 \AA). The RV measurements were obtained using the G2 numerical mask. They are reported in Table A.1 and plotted in Fig. 1.

HAT-P-17 was observed on the night of 2013/10/13, during a planetary transit. The acquisition series started before nautical twilight, while the last spectrum was taken 1.9 hr after the end of the transit, when the star was at an airmass of ~ 1.7 . During the night $\sim 73\%$ of the moon was illuminated and it was at an angular separation of $\sim 41^\circ$ from the target; we checked that no significant light contamination was present by analysing the spectra and the CCFs of the second fibre which was pointed at the sky. The resulted spectra have an average S/N of 60 (per pixel in 1-D spectra at 5500 \AA) and a G2 mask was used to measure the RVs. They are reported in Table A.2 and plotted in Fig. 2.

HAT-P-21 was observed on the night of 2014/03/07. A time-series of 36 spectra, lasting over six hours, bracketed a planetary transit from ~ 80 minutes before the ingress up to ~ 40 minutes after the egress. With an exposure time of 600 s, the spectra have

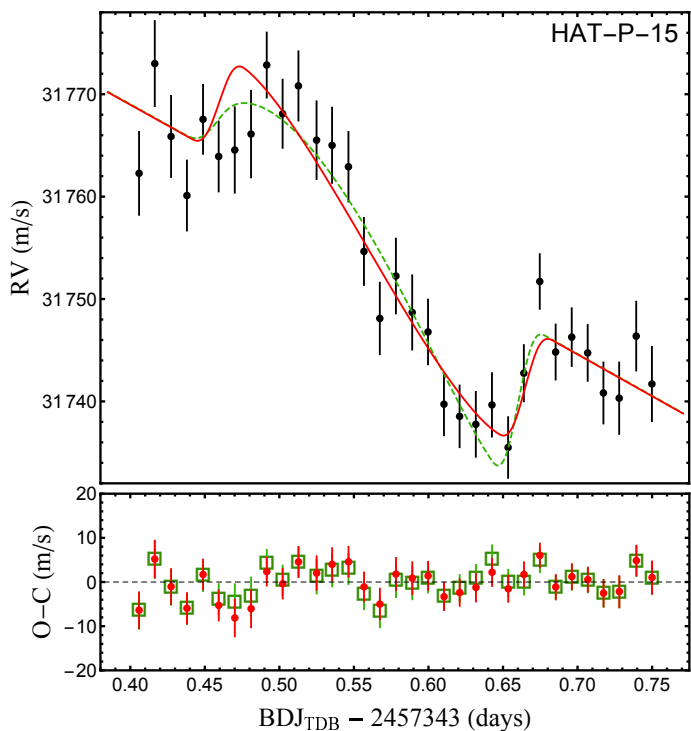


Fig. 1. RV data of the transit of HAT-P-15 b observed with HARPS-N. Superimposed are the best-fitting RV-curve models (the red line does not include the modelling of the stellar convective blueshift (CB) effect, while the green-dashed line does). The corresponding residuals are plotted in the lower panel. For clarity, the error bars are displayed only for the model without the CB effect. See the discussion in Sect. 8.2

a typical S/N of 20 (per pixel in 1-D spectra at 5500 \AA). However the last two hours of observations were affected by passing clouds, so some spectra have much lower S/N and large RV uncertainties. The RV values were obtained using a G2 mask; they are reported in Table A.3 and plotted in Fig. 3.

HAT-P-26 was observed on the night of 2015/03/26. The first spectrum was acquired about 15 minutes after the transit ingress, when the rising target was at an airmass of 1.6. The time series of 27 spectra stretched to ~ 2 hours after the transit egress. The 600 s long exposures have a typical S/N of 15 (per pixel in 1-D spectra at 5500 \AA). The last 6 spectra of the series were affected by deteriorating weather conditions. The RV values were obtained using a K5 mask; they are reported in Table A.4 and plotted in Fig. 4

HAT-P-29 was observed on the night of 2013/10/16. A series of 23 spectra spanned the time interval from ~ 1 hour before transit ingress up to ~ 1 hour after egress. With an exposure time of 900 s the spectra have an average S/N of 25 (per pixel in 1-D spectra at 5500 \AA). The sky spectra acquired with the second fibre show no detectable sign of light contamination from the full Moon. The RV values were obtained using a G2 mask. They are reported in Table A.5 and plotted in Fig. 5

3.2. Photometric follow-up observations

Except for HAT-P-15, the planetary systems studied in this work were monitored with an array of medium-class telescopes with the aim of obtaining high-quality transit light curves, which can be used for refining the physical parameters of both the star and the planet, as well as checking stellar activity. As in our previous

Table 1. Details of the spectroscopic observations of the planetary transits recorded with HARPS-N.

Object	Date ^(a)	UT Start	UT End	N_{obs}	T_{exp} [s]	Airmass ^(b)	Moon ^(c)	2 nd fibre
HAT-P-15	2015-11-16	21:29	05:59	33	900	1.62→1.02→1.59	NO	Sky
HAT-P-17	2013-10-13	19:29	01:28	23	900	1.07→1.00→1.67	73%/41°	Sky
HAT-P-21	2014-03-07	22:24	04:37	36	600	1.28→1.02→1.28	46%/85°	Sky
HAT-P-26	2015-03-26	23:48	04:30	27	600	1.60→1.10→1.17	NO	Sky
HAT-P-29	2013-10-16	00:15	06:15	23	900	1.12→1.09→1.72	96%/56°	Sky

Notes. ^(a) Dates refer to the beginning of the night. ^(b) Values at first→meridian→last exposure. ^(c) Fraction of illumination and angular distance from the target.

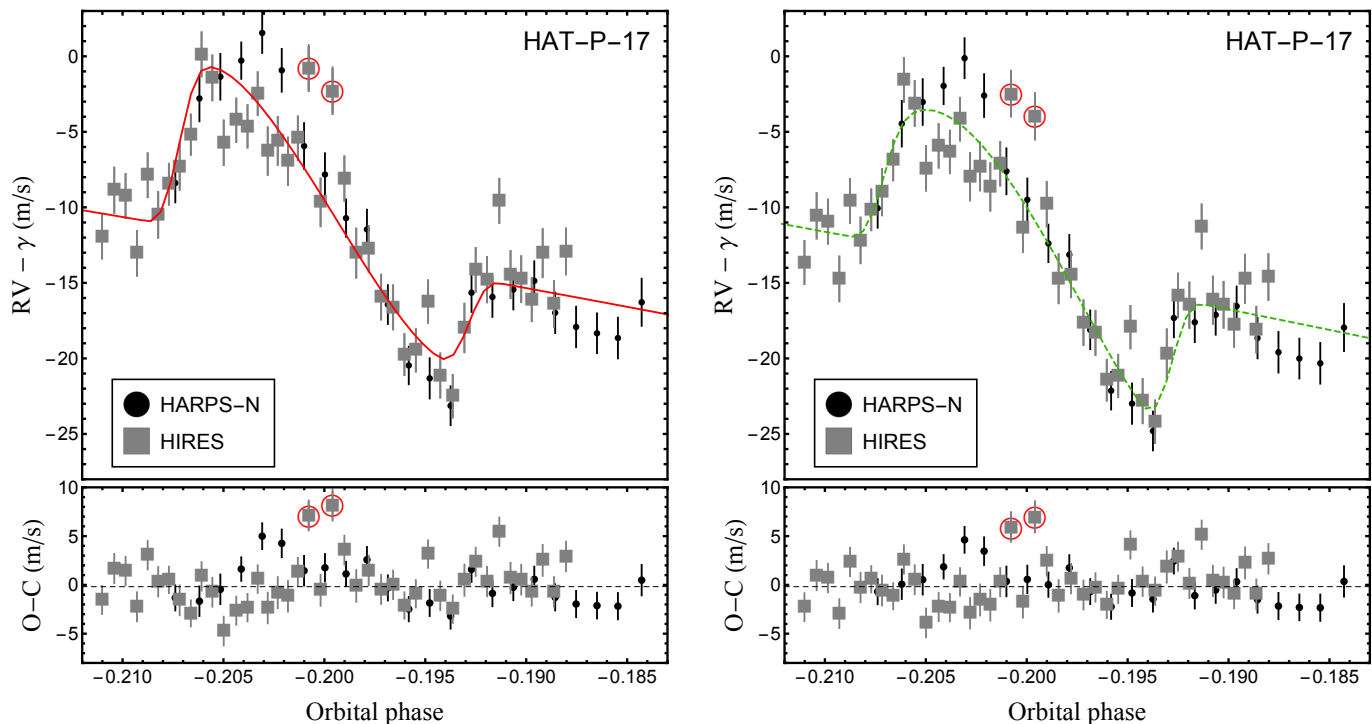


Fig. 2. A joint RV-data plot of two different transit events of HAT-P-17 b, fitted with two different models: RV only (*left-hand panels*) and RM+CB (*right-hand panels*). *Left-hand panels*: grey squares are the HIRES RVs (Fulton et al. 2013). Note that the two circled data points were considered outliers (they showed residuals larger than 4σ and, therefore, were not considered in the modelling process). Black points are the HARPS-N RVs (this work). The best-fitting values of the systemic RVs were subtracted in order to compare the two data sets. The red line represents the best-fitting model of the RM effect; the RV residuals are plotted in the lower panel. *Right-hand panels*: same as left panels but with the RM effect and CB effect modelled simultaneously (green-dashed line).

works based on photometric follow-up observations of transiting exoplanets (e.g., Southworth et al. 2012; Ciceri et al. 2013), we autoguided the telescopes and adopted the *defocussing* technique in all the observations to significantly improve the precision of the photometry. The photometric data thus obtained were reduced using a modified version of the DEFOT pipeline (Southworth et al. 2014) and the light curves were extracted by performing standard aperture photometry. For the same purpose as above, we also analysed the light curves obtained by the TESS space telescope (Ricker et al. 2015).

HAT-P-15. Having an orbital period larger than 10 d, complete transits of HAT-P-15 b are difficult to catch with ground-based facilities. Unfortunately, HAT-P-15 light curves are also not available in both the TESS 2 min and 20 s cadence target list² for sector 19. In order to check the 30 min cadence TPF files, we went to TESScut³ and downloaded the TPFs for the RA and

DEC of HAT-P-15. Having inspected the TPFs, we realised that HAT-P-15 was not observed by TESS.

HAT-P-17. HAT-P-17 b also has an orbital period larger than 10 d, so the observation of a complete transit is difficult to achieve using ground-based telescopes. We observed one incomplete transit of HAT-P-17 b on July 2012 through a Gunn-*i* filter with the BFOSC (Bologna Faint Object Spectrograph & Camera) imager, which is mounted on the Cassini 1.52 m Telescope at the Astrophysics and Space Science Observatory of Bologna in Loiano (Italy). Another incomplete transit of HAT-P-17 b was observed on July 2014 with the Calar Alto (CA) Zeiss 1.23 m telescope and using a Cousins-*I* filter. Details of the instruments and telescopes were already reported in our previous works (see, e.g., Mancini et al. 2017). Two transits were observed by TESS with the 2 min cadence during the monitoring of Sector 15 of its primary mission. Continuous observations of the target star were obtained from 2019-08-23 to 2019-09-03, for a total of 892 measurements. All the transit light curves of HAT-P-17, which were analysed in this work, are plotted in Fig. B.1.

² <https://tess.mit.edu/observations/target-lists/>

³ <https://mast.stsci.edu/tesscut/>

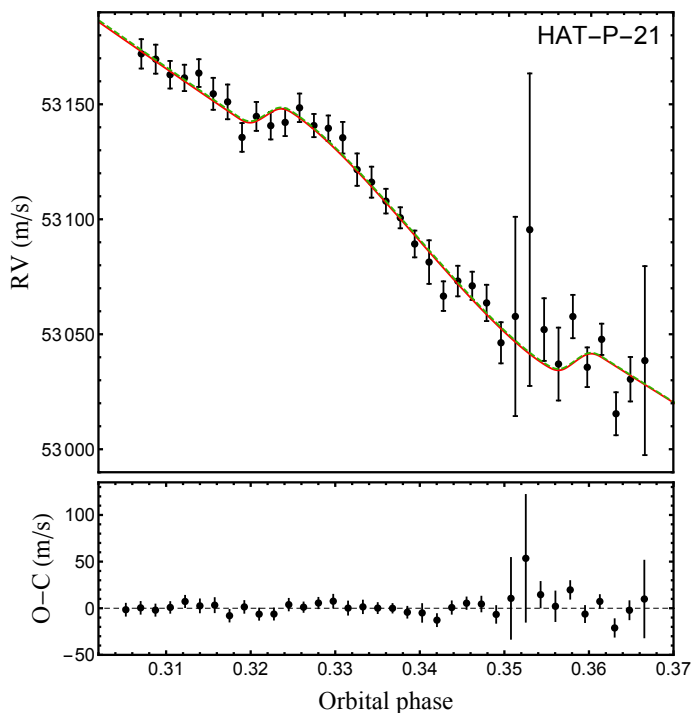


Fig. 3. RV data of the transit of HAT-P-21 b observed with HARPS-N (this work). Superimposed are the best-fitting RV-curve models (red line is without, green-dashed line with the CB effect). The corresponding residuals are plotted in the lower panel. For clarity, the error bars are displayed only for the model without the CB effect.

HAT-P-21. Two complete transit events of HAT-P-21 b were observed on March 2012 with the Cassini 1.52 m and the CA 1.23 m telescopes, through a Gunn-*r* and a Cousins-*R* filter, respectively. The first data set was severely affected by clouds (Fig. B.2.). Five transits were observed by TESS with the 2 min cadence during the monitoring of Sector 22 of its primary mission. Continuous observations of the target star were obtained from 2020-02-22 to 2020-03-14, for a total of 1777 measurements. All the transit light curves of HAT-P-21, which were analysed in this work, are plotted in Fig. B.2.

HAT-P-26. Four complete and one partial transit events of HAT-P-26 b were observed with the CA 1.23 m telescope, through a Cousins-*I* filter, between March 2012 and February 2018. They are plotted in Fig. B.3. Again, there are no TESS data for this target. It is scheduled to be observed in March 2022 in sector 50. It was missed last time due to being close to the ecliptic, but for the extended mission the orientation of TESS has been changed to observe sections of the sky that were missed.

HAT-P-29. Four transits of HAT-P-29 b were observed with the CA 1.23 m telescope, two through a Cousins-*R* filter and two through a Cousins-*I* filter. The last two were only partially observed because they occurred much later than expected. Another two incomplete transits were observed with the DOLORES⁴ instrument, mounted on the TNG, and with the IAC 80 cm telescope, through a Johnson-*R* and Cousins-*R* filter, respectively. Two complete transits were observed with the INAF-OAPd Copernico 1.82 m telescope, which is located at Cima Ekar-Asiago (Italy), using the Asiago Faint Object Spectrograph and Camera

⁴ DOLORES (Device Optimized for the LOw RESolution) is a low-resolution spectrograph and camera installed at the Nasmyth-B focus of the Telescopio Nazionale Galileo.

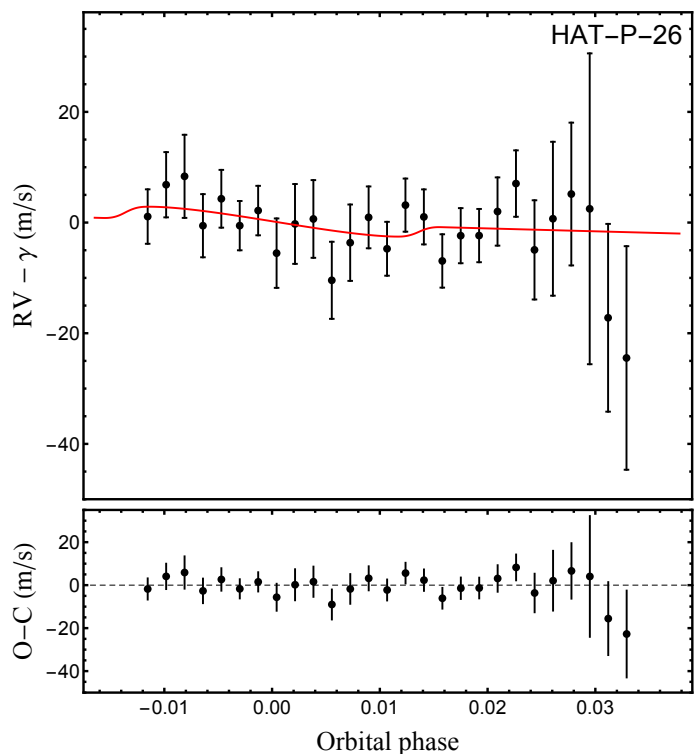


Fig. 4. RV data of the transit of HAT-P-26 b observed with HARPS-N (this work). Superimposed is the best-fitting RV-curve model without the CB effect (red line). The corresponding residuals are plotted in the lower panel.

(AFOSC) and a Sloan-*r* filter within the long-term monitoring program of the TASTE project (Nascimbeni et al. 2011). Details about the last two telescopes were already reported in our previous works (see, e.g., Covino et al. 2013; Mancini et al. 2015). Finally, four transits were observed by TESS. They are plotted in Fig. B.4.

4. Light-curve analysis

The light curves of the transit events of HAT-P-17 b, HAT-P-21 b, HAT-P-26 b and HAT-P-29 b, which were presented in the previous section, were individually modelled with the JKTEBOP code (Southworth 2013) to make a new determination of the transit parameters. This code considers stars and planets as spheres and makes use of the Levenberg-Marquardt optimisation algorithm in order to fit the parameters of the transit light curves. These are the orbital period and inclination (P_{orb} and i), the time of transit midpoint (T_0), the sum and ratio of the fractional radii, i.e. $r_{\star} = R_{\star}/a$ and $r_p = R_p/a$; R_{\star} and R_p are the radii of the star and planet, respectively, while a is the semi-major axis of the planetary orbit. For modelling the limb darkening (LD) of the star, we used a quadratic law and fitted the LD coefficients (u_{\star} and v_{\star}), taking into account the differences between the atmospheric properties of the four stars as well as the filters that were used. We also took into account the eccentric orbit of the four planets, as it has a slight effect on the shape of the transit light curves (Kipping 2008). JKTEBOP allows the inclusion of the eccentricity, e , and periastron longitude, ω , as fitted parameters constrained by their known values and uncertainties (Southworth et al. 2009), which are summarised in Table 2.

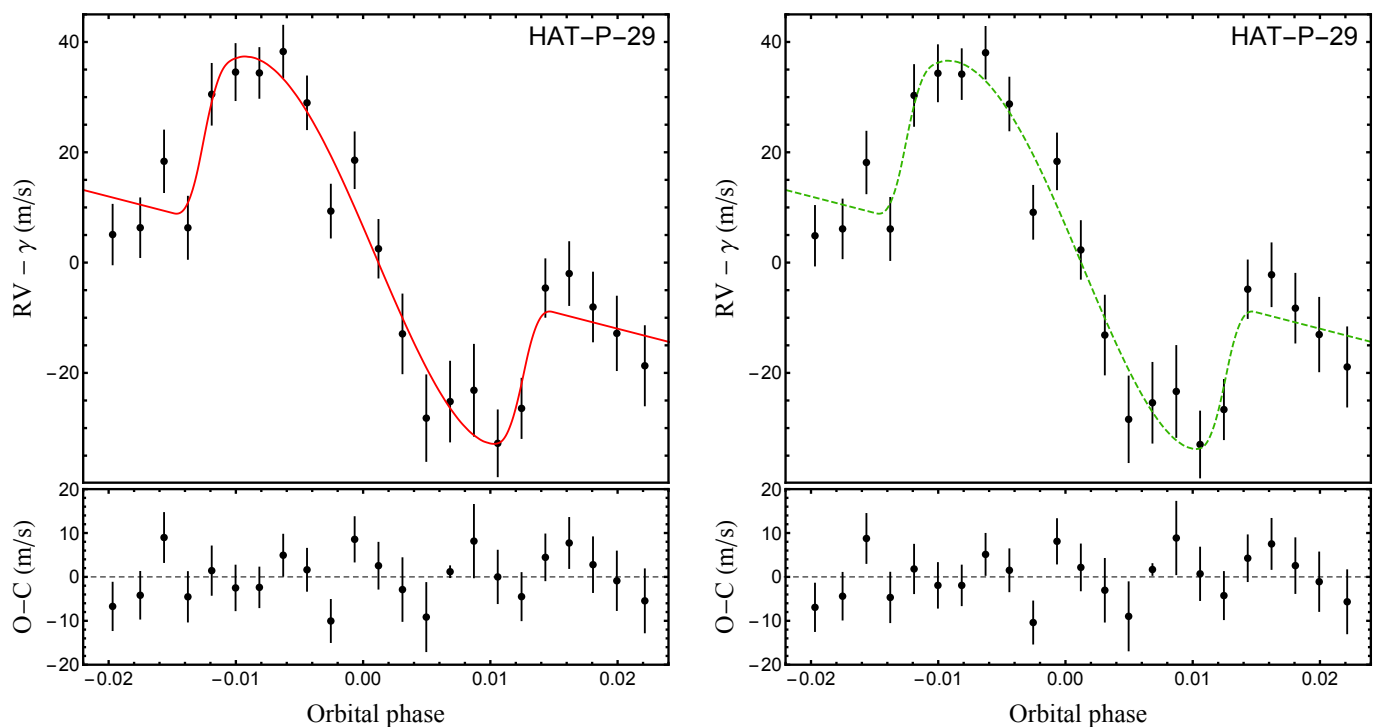


Fig. 5. *Left-hand panels:* RV data of the transit of HAT-P-29 b observed with HARPS-N (this work). The red line represents the best-fitting model of the RM effect; the RV residuals are plotted in the lower panel. *Right-hand panels:* same as left panels but with the RM effect and CB effect modelled simultaneously (green-dashed line).

Table 2. Summary of the values of two orbital elements of the five systems analysed in this work.

Planet	e	ω (deg)	Reference
HAT-P-15 b	$0.200^{+0.026}_{-0.028}$	$262.5^{+2.4}_{-2.9}$	Bonomo et al. (2017)
HAT-P-17 b	0.3417 ± 0.0036	200.5 ± 1.3	Bonomo et al. (2017)
HAT-P-21 b	0.217 ± 0.010	$305.8^{+2.1}_{-1.9}$	Bonomo et al. (2017)
HAT-P-26 b	0.124 ± 0.060	54 ± 165	Hartman et al. (2011)
HAT-P-29 b	$0.104^{+0.021}_{-0.018}$	159^{+20}_{-16}	Bonomo et al. (2017)

Finally, to mitigate the correlated (red) noise, which generally affects time-series photometry obtained by the *APER* routine⁵, we inflated the error bars of the photometric measurements so that each transit light curve had a reduced chi-square of $\chi^2_{\nu} = 1$ during the best-fitting process. The light curves and the corresponding *JKTebop* best-fitting models are reported in Figs. B.1–B.4.

The uncertainties of the fitted parameters were estimated by running both a Monte Carlo and a residual-permutation algorithm. For each of the light curves, we ran 10 000 simulations for the Monte Carlo algorithm and the maximum number of simulations (which is one less than the number of data points) for the residual-permutation algorithm. We took the largest of the two 1σ values as the uncertainty for each parameter. Finally, for each planetary system, the final values of each parameter were calculated by taking the weighted average of the values extracted from the fit of all the individual light curves; the relative uncertainties were used as weights. These values are shown in the Tables reported in Appendix D and are in good agreement with those available in the literature.

5. Orbital period determination

In the modelling of the transit light curves with *JKTebop*, we also estimated each transit mid-time and placed them on the BJD (TDB) time system. By joining these new measurements with those already published, it is possible to review and refine the orbital ephemerides for the HAT-P-17, HAT-P-21, HAT-P-26 and HAT-P-29 planetary systems, as well as search for possible TTVs due to variations in the planetary orbital period. The timings that we used for each of the four systems and their residuals for a constant period are shown in the Tables reported in Appendix C.

HAT-P-17. The few transit timings recorded for HAT-P-17 b do not allow us to perform any detailed investigations about possible TTVs. Besides the timing from the discovery paper (Howard et al. 2012), we only have two from partial transit observations and two more from TESS observations. Assuming that the orbital period is constant (linear model), we performed a weighted linear least-squares fit to the mid-transit times versus their cycle number, i.e.

$$T_{\text{mid}} = T_0 + P_{\text{orb}} E, \quad (1)$$

where E is the number of orbital cycles after the reference epoch T_0 . The fit returned

$$T_{\text{mid}} = \text{BJD}_{\text{TDB}} 2\,454\,801.16943(15) + 10.33853781(60) E, \quad (2)$$

with a $\chi^2_{\nu} = 0.48$ (the quantities in brackets represent the uncertainties in the preceding digits). The residuals of the timings of mid-transit are plotted in Fig. C.1.

HAT-P-21. Also for HAT-P-21 b, few transit mid-times are available and we can not investigate possible TTVs. Of the two transit light curves we have obtained, one is of low quality with large uncertainties (Fig. B.2) so was excluded from the analysis. This

⁵ *APER* is part of the *ASTROLIB* subroutine library distributed by NASA.

left us with only seven timings: one from the discovery paper (Bakos et al. 2011), one from our observational program and five from TESS. The linear fit gives

$$T_{\text{mid}} = \text{BJD}_{\text{TDB}} 2\,454\,996.41243(60) + 4.12449009(90)E, \quad (3)$$

with a $\chi^2_{\nu} = 1.05$. The residuals of the timings of mid-transit are plotted in Fig. C.1.

HAT-P-26. This system is a special case for orbital period determination. Hartman et al. (2011) found a variation in the systemic velocity with a detection significance of 2.1σ . Stevenson et al. (2016) noted that there appeared to be a curvature in the diagram of the residuals from fitting a linear ephemeris to the measured times of minimum light. This was followed up by von Essen et al. (2019), who found clear evidence for a sinusoidal variation with a period of 270 epochs (1140 d) and an amplitude of 4 min. They tentatively attributed this to the presence of a third body, in agreement with the marginal detection of a variable systemic velocity.

We assembled the times of mid-transit from previous works (see the list compiled by von Essen et al. 2019) and augmented these with our own measurements. We then fitted four types of orbital ephemeris to them: linear, quadratic, cubic, and linear plus sinusoid. The last ephemeris was modelled with the equation

$$T_{\text{mid}} = T_0 + P_{\text{orb}}E + A \sin\left(\frac{2\pi E}{P_{\text{sine}}} - \phi\right), \quad (4)$$

where P_{sine} is the period of the sine wave (in units of the orbital period), A is the sine amplitude and ϕ is the phase offset with respect to T_0 . We were initially unable to find a good fit, with a best value of $\chi^2_{\nu} = 2.7$. A close inspection of the published timings showed that three of them have implausibly small errorbars of 0.000011 to 0.000016 d (1.0 to 1.4 s). These three are based on transmission spectroscopy with HST (Wakeford et al. 2017) and contain large gaps due to the low-Earth orbit: all fully cover the egress but have no observations during ingress.

We therefore increased the errorbars of all four timings from Wakeford et al. (2017) by a factor of ten and refitted the full set of timings (a reanalysis of the HST data to obtain improved timings and uncertainties is outside the scope of the current work but would be useful in future studies). The factor of ten was chosen iteratively and is the factor by which the errorbars from Wakeford et al. (2017) must be increased by to get the sum of the absolute values of the residuals of these four datapoints to be equal to 4σ (i.e. the multiplicative factor was determined from the scatter of the data around the best fit instead of the quoted errorbars).

With these revised error bars, we find decent fits for all four types of orbital ephemeris. The sinusoidal model fits the data best and is in good agreement with that from von Essen et al. (2019) and is also supported by our new transit timings. In Table 3 we provide the fitted parameters, uncertainties, and Bayesian and Akaike Information Criterion (BIC and AIC) values for the four ephemerides. The sinusoidal variation is confirmed with an amplitude significant at a level of 6σ and much better BIC and AIC values. We therefore confirm that the HAT-P-26 system shows transit timing variations; see Fig. 6.

Interpreting the oscillating $O - C$ as a light time effect, we find a projected semi-major axis of the orbit of the star-planet system around the centre of mass with the third body $a_1 \sin i \sim 0.186 \pm 0.030$ au and a mass function in solar units $(a_1 \sin i)^3 / P_{\text{cyc}}^2 = (6.3 \pm 4.3) \times 10^{-4} \text{ au}^3 \text{ yr}^{-2}$, where $P_{\text{cyc}} =$

1167 ± 39 days is the $O - C$ modulation period. This corresponds to a minimum mass of the third body $M_{\text{TB}} \sim 0.07 M_{\odot}$ assuming $M_{\text{TB}} \ll M_s$, where M_s is the mass of HAT-P-26. In the most favourable conditions, the angular separation of the third body from HAT-P-26 is only 14 mas, making its direct detection challenging, especially if it is a very faint brown dwarf as expected if it has the same age as estimated for the star. Nevertheless, the third body hypothesis is apparently in conflict with the barycentre acceleration of the HAT-P-26 system as measured by Hartman et al. (2011) because our model predicts a mean minimum acceleration of $|\dot{\gamma}| \sim 2.2 \text{ m s}^{-1} \text{ day}^{-1}$ along the time interval of 182.69 days covered by their observations, while they gave $\dot{\gamma} = -0.028 \pm 0.014 \text{ m s}^{-1} \text{ day}^{-1}$. An alternative hypothesis to explain the observed $O - C$ modulation is the perturbation of the orbit of HAT-P-26 b by a distant third body as discussed in Sect. 4 of Agol et al. (2005). Their model requires an eccentric orbit of the third body which is associated with a non-sinusoidal shape of the $O - C$ modulation. We find a minimum eccentricity $e = 0.67$ for the minimum third body mass as estimated from the mass function. Lower values of the eccentricity require a larger third body mass; for example, $e = 0.33$ requires a mass four times the minimum mass. Another kind of TTV model based on an exchange of angular momentum between the orbit and the rotation of the planet, as suggested by Lanza (2020), is disfavoured by the small moment of inertia of the planet that does not allow to store enough angular momentum to account for the amplitude of the $O - C$ modulation.

HAT-P-26 is astrometrically well-behaved according to the Gaia EDR3 archive information (Gaia Collaboration 2016, 2021): both the values of astrometric excess noise (0.10 mas) and of renormalized unit weight error (RUWE = 1.04) indicate that a single-star solution fits well the available astrometric data. Hot-Jupiter hosts harboring known or likely long-period, massive companions typically have RUWE $\gtrsim 1.1$ (e.g., Belokurov et al. 2020), but these are not expected to be the ones responsible for the possible TTVs observed in the HAT-P-26 photometry.

We conclude that what seems to be a cyclic TTV in the HAT-P-26 system is worthy of further investigation by collecting more times of mid-transit. This will allow us to look for a non-sinusoidal shape of the modulation and to refine its period and amplitude before we can draw any sound conclusion on its origin.

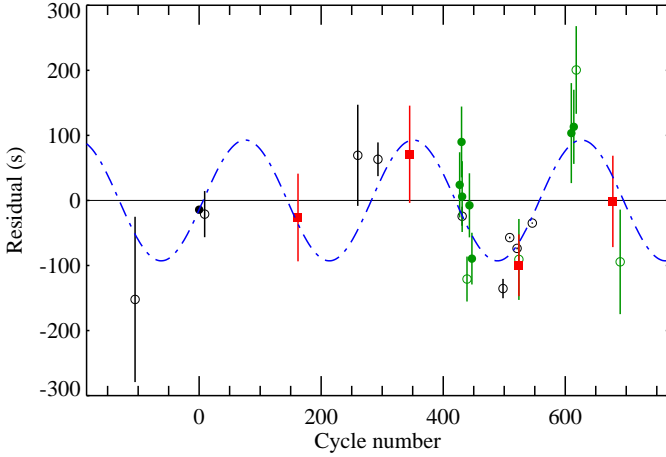
HAT-P-29. Photometric follow-up of HAT-P-29 b transit events were performed by Wang et al. (2018) and Mallonn et al. (2019). In particular, Mallonn et al. (2019) recorded two incomplete transit light curves with the Stella 1.2 m telescope at the Izana Observatory, while Wang et al. (2018) reported the observations of one complete and six incomplete transit light curves with the Schmidt telescope at the Xinglong Station; these authors also observed a complete light curve with the 1 m telescope operated at the Weihai Observatory. All these light curves have point-to-point scatters larger than 2 mmag.

The two timings reported by Mallonn et al. (2019) are early by about 900 s. Since they were both based on transit events in which the egress was not observed, their reliability is reduced (e.g., Gibson et al. 2009) and we decided to exclude them from the analysis.

We joined our new timings (see Fig B.4) with that from the discovery paper (Buchhave et al. 2011) and the eight ones from Wang et al. (2018), obtaining a total of 18 mid-transit times. We tried to model the data by using both a linear and a quadratic

Table 3. Parameters of the four ephemerides fitted to the measured times of mid-transit in the HAT-P-26 system. Quantities in brackets represent the uncertainties in the final digits of the preceding numbers.

Quantity	Linear	Quadratic	Cubic	Sinusoidal
T_0 (BJD/TDB)	2455304.652182 (32)	2455304.652181(32)	2455304.652180 (29)	2455304.65234 (35)
Linear term (d)	4.23450158 (18)	4.2345025 (15)	4.2345179 (43)	4.23450213 (76)
Quadratic term (d)		$(-1.8 \pm 2.7) \times 10^{-9}$	$(-6.7 \pm 1.7) \times 10^{-8}$	
Cubic term (d)			$(6.7 \pm 1.8) \times 10^{-11}$	
Sine period (epochs)				275.5 ± 9.1
Sine amplitude (s)				93 ± 15
Sine phase (BJD/TDB)				0.15 ± 0.33
χ^2_ν	1.67	1.66	1.40	1.07
AIC	73.3	74.6	56.9	32.5
BIC	75.8	78.3	61.7	35.0
rms of the residuals (s)	91.0	91.4	83.1	56.7


Fig. 6. Plot of the residuals of the timings of mid-transit of HAT-P-26 b versus the linear term in the sinusoidal ephemeris. The dotted blue line shows the sine curve and the points represent the residuals of the measured transit times versus the linear term in the ephemeris. Filled green circles are data from von Essen et al. (2019), black circles are other timings from the literature that are also reported in von Essen et al. (2019), and red squares are the new timings from this work. Empty circles refer to mid-transit times estimated from incomplete transit light curves. The errorbars of the timings coming from incomplete HST light curves were increased (see text).

ephemeris, the latter in the form

$$T_{\text{mid}} = T_0 + P_{\text{orb}}E + \frac{1}{2} \frac{dP_{\text{orb}}}{dE} E^2, \quad (5)$$

where $\frac{dP_{\text{orb}}}{dE}$ is the change in the orbital period between succeeding transits. The fit of the mid-transit times with a straight line gave

$$T_{\text{mid}} = \text{BJD}_{\text{TDB}} 2\,455\,838.59462 (61) + 5.7233746 (32) E, \quad (6)$$

with a $\chi^2_\nu = 6.4$ and a root-mean-square deviation (rmsd) scatter of 244 s. The residuals are plotted in Fig. C.1. Instead, the best-fitting quadratic ephemeris returned

$$T_{\text{mid}} = \text{BJD}_{\text{TDB}} 2\,455\,838.59442 (59) + 5.7233823 (59) E + (-2.4 \pm 1.6) \times 10^{-8} E^2, \quad (7)$$

with a $\chi^2_\nu = 5.6$ and rmsd = 267 s. We also estimated the Akaike Information Criterion (AIC) and the Bayesian Information Criterion (BIC). Both these criteria slightly prefer the quadratic model

over the linear one. The rms is larger for the quadratic ephemeris versus the linear one only because it does not depend on the errorbars of the measured transit time. As in previous works of our series (e.g., Southworth et al. 2012; Mancini et al. 2013) such large values of the χ^2_ν should not be interpreted as a suggestion of TTVs, but as an indication that the uncertainties in the various T_0 measurements are too small. As a matter of fact, if we exclude from the analysis the five timings measured by Wang et al. (2018) from noisy data covering only part of transits, both the fits have a lower and similar reduced chi-square. We found $\chi^2_\nu = 3.9$ and rmsd = 249.7 s for the linear model and $\chi^2_\nu = 3.9$ and rmsd = 222.0 s for the quadratic model. This time, both the AIC and BIC criteria prefer the linear model over the quadratic one.

In conclusion, considering the amount of available data and their quality, we did not find a clear indication of the existence of TTVs. Further investigation needs more photometric follow-up observations of transits by HAT-P-29 b. We stress that the new linear ephemeris that we determined (Eq. 6; Fig. C.1) is such that the orbital period is 16.3 ± 4.5 seconds longer than that of the discovery paper, in good agreement with what was found by Wang et al. (2018).

6. Frequency analysis of the time-series light curves

Knowledge of the stellar rotational period P_{rot} is important for better characterization of a star-planet system. In particular, by combining the value of P_{rot} with those of the stellar radius R_* and projected rotational velocity $v \sin i_*$, we can determine the inclination of the stellar spin axis i_* . In turn, i_* , together with the projected spin-orbit misalignment angle λ , yields an estimation of the true obliquity angle ψ (Winn et al. 2007).

We have analysed the HATNet photometric data⁶ to look for possible periodic variations induced by activity and modulated by stellar rotation. We applied the Trend Filtering Algorithm (TFA; Kovács et al. 2005) to the photometric time-series produced by the HATNet pipeline and examined all three data sets corresponding to different apertures.

HAT-P-15 was observed on 106 different nights between September 2005 and February 2006. The typical standard deviation of photometric measurements within the same night is $\sigma \sim 9$ mmag. Nightly averaged photometric values have very

⁶ The original HATNet lightcurves are publicly available at <https://hatnet.org/planets/discovery-hatlcs.html>

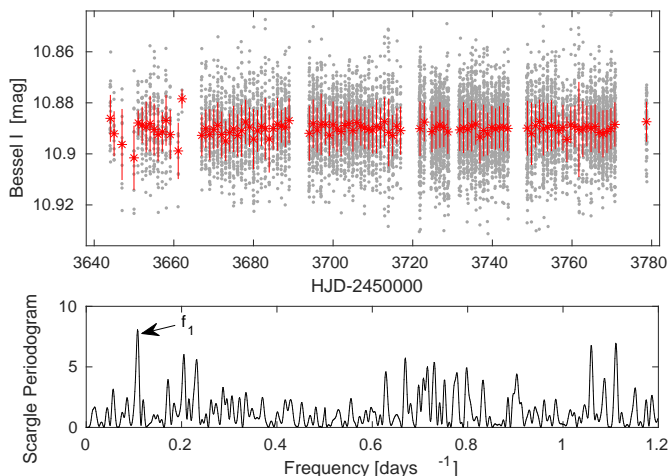


Fig. 7. Top panel: HATNet photometric time series of HAT-P-15. Grey points are the original TFA3 data set, red asterisks are the data binned on a nightly base. Bottom panel: Scargle periodogram of the original data set.

small dispersion ($\sigma \sim 2$ mmag), indicating that the star had a low activity level (see the upper panel in Fig. 7). After removing in-transit data points (190 out of 8945), we calculated the Scargle periodogram (see the bottom panel in Fig. 7) and found that the highest peak occurs at $P_1 \equiv 1/f_1 = 9.3$ days. By using the bootstrap method, we estimated for the peak at P_1 a false alarm probability (FAP) of 7.6% and concluded that it is not statistically significant.

HAT-P-17 was monitored by four different telescopes of the HAT network from June 2004 to October 2005 for a total of ~ 250 nights. Within the same night, photometric measurements have an average standard deviation of $\sigma \sim 6$ mmag. We have considered first the full dataset and then, independently, the first and last longer observing seasons with red asterisks and blue circles respectively); in no case does the periodogram analysis show significant peaks. The low dispersion ($\sigma = 1.8$ mmag) of the nightly binned photometry indicates a very low activity level.

HAT-P-21 was monitored from November 2006 to June 2008, for a total of 24633 single measurements. The power spectrum of the 288 daily means clearly shows two peaks at $f = 0.063$ d $^{-1}$ and $2f = 0.126$ d $^{-1}$ (Fig. 8, top panel). Interpreting the signal as due to the stellar rotation, we searched for the best fit by fixing simultaneously the frequency f and its harmonic $2f$, thus obtaining $P_{\text{rot}} = 15.88 \pm 0.02$ days. The folded light curve shows a flat part and a full-amplitude of 7.1 mmag (Fig. 8, bottom panel). Since the noise level in the power spectrum corresponds to 0.28 mmag, the signal has to be considered highly significant ($S/N = 12.7$).

HAT-P-26 was observed from January to August 2009, for a total of 12223 measurements. The frequency analysis of the 150 daily means does not show any significant peak above the noise level of 0.21 mmag.

HAT-P-29 was observed from October 2008 to March 2009, for a total of 3128 measurements. The frequency analysis of the 76 daily means does not show any significant peak above the noise level of 0.25 mmag.

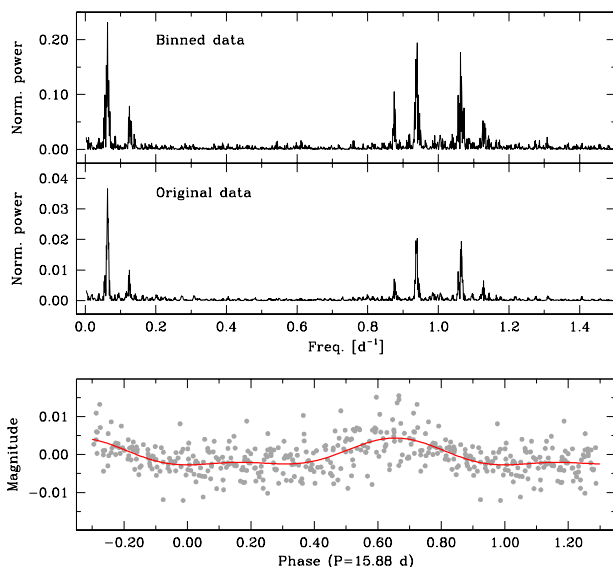


Fig. 8. Detection of the rotational period of HAT-P-21. *Top panel:* power spectrum of the photometric measurements. The first two peaks corresponding to $f = 0.063$ d $^{-1}$ and $2f$, while the other peaks are their aliases. *Bottom panel:* photometric measurements (in grey) folded with $P_{\text{rot}} = 15.88$ days. The error bars have been suppressed for clarity.

7. Analysis of stellar parameters

We fit the Spectral Energy Distribution (SED) via the MESA Isochrones and Stellar Tracks (MIST) (Dotter 2016; Choi et al. 2016) through the EXOFASTv2 suite (Eastman et al. 2019). We fit the available archival magnitudes imposing gaussian priors on T_{eff} and $[\text{Fe}/\text{H}]$ based on spectroscopic measurements and on parallax π based on the Gaia EDR3 astrometric measurement (Gaia Collaboration 2016, 2021); this astrometric prior helps constraining the stellar radius and improves the precision of the stellar parameters resulting from the SED fitting procedure. The stellar parameters were simultaneously constrained by the SED and the MIST isochrones, as the SED primarily constrains R_* and T_{eff} , and a penalty for straying from the MIST evolutionary tracks ensures that the resulting star is physical in nature. The results are shown in the Tables reported in Appendix D and they were used for the best-modelling fit of the RM effects (Sect. 8.2) as well as for reviewing the physical parameters of the systems (Sect. 9).

8. HARPS-N spectra analysis

8.1. Stellar atmospheric parameters

Stellar atmospheric parameters were derived using the weighted means of all HARPS-N spectra available for the five targets. We therefore measured the equivalent widths (EWs) of iron lines taken from the list by Biazzo et al. (2015), and, together with the *abfind* driver of the MOOG code (Snedden 1973, version 2013) and the Castelli & Kurucz (2003) grid of model atmospheres, we obtained effective temperature (T_{eff}), surface gravity ($\log g$), microturbulence velocity (ξ), and iron abundance ($[\text{Fe}/\text{H}]$). In particular, we imposed the independence of the iron abundance on the line excitation potentials (for T_{eff}) and EWs (for ξ), and the ionization equilibrium between Fe I and Fe II (for $\log g$). All the analysis was performed differentially with respect to the Sun, thanks to a mean Vesta spectrum acquired with HARPS-N.

Table 4. Stellar atmospheric parameters determined from HARPS-N spectra.

Object	T_{eff} (K)	$\log g$ (dex)	ξ (km s^{-1})	[Fe/H] (dex)	$v \sin i_{\star}$ (km s^{-1})
HAT-P-15	5620 ± 20	4.45 ± 0.15	0.77 ± 0.18	$+0.24 \pm 0.10$	2.3 ± 0.5
HAT-P-17	5350 ± 20	4.55 ± 0.20	0.80 ± 0.30	$+0.02 \pm 0.09$	0.5 ± 0.5
HAT-P-21	5695 ± 45	4.28 ± 0.15	0.98 ± 0.05	$+0.04 \pm 0.09$	3.5 ± 0.5
HAT-P-26	5100 ± 20	4.51 ± 0.13	0.30 ± 0.30	$+0.05 \pm 0.10$	1.9 ± 0.4
HAT-P-29	6140 ± 30	4.39 ± 0.14	1.27 ± 0.02	$+0.25 \pm 0.08$	4.5 ± 0.8

After fixing the stellar parameters (T_{eff} , $\log g$, ξ , [Fe/H]) at the values derived through the iron line EWs, we applied the spectral synthesis method to derive the projected rotational velocity ($v \sin i$), as done in Barbato et al. (2019). We therefore considered two spectral regions around 6200 and 6700 Å and used both the *synth* driver of the same MOOG code and the model atmospheres.

We refer to the mentioned papers (and references therein) for further details on the procedures. The final results of the spectroscopic analysis applied here to determine the stellar atmospheric parameters are listed in Table 4.

8.2. Determination of the spin-orbit alignment

The modelling and fitting of the RV measurements were performed by using a code that we developed within the MATLAB software *ambient*⁷. A thorough description of the code was already given in Esposito et al. (2017). Practically, we derive the best-fitting values for three parameters: the stellar projected rotational velocity $v \sin i_{\star}$, the systemic RV γ and the sky-projected orbital obliquity angle λ . The other pertinent parameters (see Esposito et al. 2017) are kept fixed to the values found in the photometric and spectroscopic analysis, while their uncertainties are propagated for determining the error bars of $v \sin i_{\star}$, γ and λ . We have upgraded the code to include the possibility to model and fit the effect of the stellar convective blueshift (CB) on the in-transit RV curve; we used a simple one-parameter model introduced by Shporer & Brown (2011). The results of the fits are summarised in Table 5, while the best-fitting RV models are shown in Figs. 1, 2, 3, 4 and 5, superimposed on the data points.

HAT-P-15. For this target, we only have the RV time-series spanning one transit and no photometric follow-up observations. Therefore, for many relevant parameters, we had to adopt values from the literature as well as from our analysis of the stellar parameters (see Sect. 7 and Table D.1). The free parameters in our fit are λ , $v \sin i_{\star}$ and γ . Since the uncertainties on the ephemerides reported in Kovács et al. (2010) propagated to an uncertainty of 10 minutes on the mid-transit time at the epoch of our observations, we also included the time of periastron as a free parameter.

We considered both models with and without the CB effect and show the results of the fits in Fig. 1. We used the Bayesian Information Criterion (BIC) to compare the two models. With $\Delta\text{BIC} = -0.95$, the model with CB is only marginally better. The best fit value of $\text{CBV} = -1.40 \pm 0.85 \text{ km s}^{-1}$ is suspiciously high for a G5 star (Dravins 1990), and we think it is driven by the first three in-transit data points. Therefore we prefer to adopt

⁷ MATLAB R2015b, Optimization Toolbox 7.3 and Curve Fitting Toolbox 3.5.2, The MathWorks, Inc., Natick, Massachusetts, United States.

Table 5. Parameters from the best-fitting models of the RM effect for the five planetary systems.

Object	λ (degree)	$v \sin i_{\star}$ (km s^{-1})	γ (km s^{-1})	CBV (km s^{-1})
HAT-P-15	25 ± 23	1.58 ± 0.29	31.7627 ± 0.0014	-1.40 ± 0.85
	13 ± 6	1.53 ± 0.25	31.7622 ± 0.0009	–
HAT-P-17	-27.5 ± 6.7	0.84 ± 0.07	20.3141 ± 0.0021	-0.46 ± 0.11
	-41.1 ± 3.6	1.00 ± 0.09	20.3125 ± 0.0021	–
HAT-P-21	-0.5 ± 12.4	3.9 ± 0.9	-53.018 ± 0.005	undetected
	-0.7 ± 12.5	3.9 ± 0.9	-53.018 ± 0.005	–
HAT-P-26	18 ± 49	–	–	–
HAT-P-29	-21 ± 28	5.1 ± 0.9	-21.6511 ± 0.0020	> -0.58
	-26 ± 16	5.2 ± 0.7	-21.6513 ± 0.0019	–

Notes. Except for the first, the columns contain two values. Those on the top are from the fit in which we considered the stellar convective blueshift (CB), whereas those on the bottom did not. The preferred values are given in bold font for each target; see the text for details. Due to the low quality of the HAT-P-26 data, we were not able to well constrain λ for this system, which was merely estimated by fixing the value of $v \sin i_{\star}$.

the best fit values of the model without the CB effect, for which $\lambda = 13^{\circ} \pm 6^{\circ}$.

HAT-P-17 was already observed with the Keck/HIRES for detecting the RM effect, as reported by Fulton et al. (2013). Due to the slow stellar rotational velocity ($v \sin i_{\star} = 0.56^{+0.12}_{-0.14} \text{ km s}^{-1}$), they estimated the amplitude of the RM effect to be only $\sim 7 \text{ m s}^{-1}$. As a consequence, they remarked on the need to model also the effect of the CB in order to derive a correct estimation of λ . Indeed, without the CB effect modelling, they obtained $\lambda = 37 \pm 12 \text{ deg}$, whereas with the CB effect they found $\lambda = 19^{+14}_{-16} \text{ deg}$, and a CB velocity parameter $\text{CBV} = -0.65 \pm 0.23 \text{ km s}^{-1}$.

First, we used our code to make an independent fit of the HIRES RVs. Without modelling the CB effect, we obtained $\lambda = -28 \text{ deg}$ and $v \sin i_{\star} = 0.8 \text{ km s}^{-1}$; accounting for the CB effect we derived $\lambda = -17 \text{ deg}$, $v \sin i_{\star} = 0.7 \text{ km s}^{-1}$, and $\text{CBV} = -0.33 \text{ km s}^{-1}$. Provided that Fulton et al. (2013) are most likely using a different convention for the sign of λ (compare their Fig. 3 with our Fig. 2), our results are compatible with theirs: considering the CB effect results in a value of λ closer to zero. However we obtain a significantly smaller value for CBV. Unlike Fulton et al. (2013), we have rejected two of their data points as outliers (see Fig. 2) because they showed residuals larger than 4σ . Correspondingly, we find a value for the CBV closer to zero, that is $\text{CBV} = -0.33 \text{ km s}^{-1}$. Instead, by including all the data points, our best-fitting value for the CBV is -0.58 km s^{-1} , which is similar to the result found by Fulton et al. (2013).

Next, we analysed our HARPS-N RV data set, by using the same approach as for the HIRES data. The best fit values, without the CB effect, are $\lambda = -55 \text{ deg}$ and $v \sin i_{\star} = 1.6 \text{ km s}^{-1}$. By modelling also the CB effect, we obtained $\lambda = -37 \text{ deg}$, $v \sin i_{\star} = 1.1 \text{ km s}^{-1}$, and $\text{CBV} = -0.57 \text{ km s}^{-1}$. Although with a marginal statistical significance, both for HIRES and HARPS-N data sets the model including the CB effect is to be preferred, as we obtain smaller BIC: $\Delta\text{BIC} = -0.9$ and -4.1 for HIRES and HARPS-N, respectively.

Finally, we made a combined fit of the HIRES and HARPS-N RVs, and estimated the uncertainties on the best-fit parameters using the bootstrap method. The best-fit RV curve models are displayed, together with the RV data sets, in Fig. 2. The

left panels shows the model considering the RM effect only, whereas the model in the right panels accounts also for the CB effect. In the first case we derive $v \sin i_{\star} = 1.00 \pm 0.09 \text{ km s}^{-1}$, $\lambda = -41.1 \pm 3.6 \text{ deg}$, while in the second case we obtain $\text{CBV} = -0.46 \pm 0.11 \text{ km s}^{-1}$, $v \sin i_{\star} = 0.84 \pm 0.07 \text{ km s}^{-1}$, $\lambda = -27.5 \pm 6.7 \text{ deg}$. Also for the combined fit, the model that includes the CB effect is to be preferred as we obtain $\Delta\text{BIC} = -6.7$. We adopt this latter value as our final estimation of λ for HAT-P-17b.

HAT-P-21 For this target, we adopted all the planetary and stellar relevant parameters as obtained from the analysis of the light curves and the stellar spectra (see Table D.3). The best-fitting values of the parameters determined by the analysis of the in-transit RV curve are reported in Table 5. In particular, we obtained $\lambda = -0.7^{\circ} \pm 12.5^{\circ}$.

The fit using the model which include the CB effect gives a value of CBV very close to zero, and correspondingly the other fitted parameters have the same values as in the fit without CB. We notice that HAT-P-21 b has an impact parameter of $b = 0.62$, i.e. the planet never occults the central part of the stellar disk and therefore we expect the RV variations due to the CB effect to be small. We conclude that the data do not have the quality needed for a solid detection of the CB effect.

As we know the rotational period of its parent star (see Sect. 6), we are able to estimate the quantity i_{\star} using the following equation

$$P_{\text{rot}} \approx \frac{2\pi R_{\star}}{v \sin i_{\star}} \sin i_{\star}, \quad (8)$$

which resulted to be $62^{\circ} \pm 16^{\circ}$. Knowing i_{\star} , i and λ , we can calculate the true misalignment angle via (Winn et al. 2007)

$$\cos \psi = \cos i_{\star} \cos i + \sin i_{\star} \sin i \cos \lambda. \quad (9)$$

The value that we obtained is $\psi = 25^{\circ} \pm 16^{\circ}$.

HAT-P-26 Based on published ephemerides, the first point of the HARPS-N time-series observations was taken ~ 15 minutes after the transit had already started. Instead, the last points present a large scatter due to worsening weather conditions (see Fig. 4). Therefore, the fit of the data does not allow to constrain λ at the required precision as in the other four cases presented in this work. We made a putative estimate of λ by fixing the value of $v \sin i_{\star}$ to that estimated from the spectroscopy (see Table 4) and finding $\lambda = 18^{\circ} \pm 49^{\circ}$, which suggests a a prograde orbit for HAT-P-26 b.

HAT-P-29 We find that the fit of the data using a model which includes the CB effect is slightly disfavoured with respect to the fit without CB ($\Delta\text{BIC} = 3.0$); given the relatively large value of $v \sin i_{\star} = 5.2 \text{ km s}^{-1}$, we expected that the CB effect can only have a minor impact on the shape of the in-transit RV curve. Therefore, for HAT-P-29 we adopt the results of the fit without CB, that is $\lambda = -26^{\circ} \pm 16^{\circ}$. However, the analysis of the fit with the CB provides us with a useful 1σ lower limit ($> -0.58 \text{ km s}^{-1}$) to the value of CBV.

9. Physical parameters

Considering the new photometric data available for HAT-P-17, HAT-P-21, HAT-P-26 and HAT-P-29, we reviewed the physical properties of these planetary systems. We followed the *Homogeneous Studies* approach (Southworth et al. 2012 and references therein) and combined the parameters obtained from the light

curves and spectroscopic observations, placing constraints on the properties of the host stars, which we can deduce from theoretical evolutionary models of stars. In particular, we used the following spectroscopic properties of the host stars, which we obtained from the analysis of the stellar spectra (see Sect. 8): the projected rotational velocity $v \sin i_{\star}$, the effective temperature T_{eff} , the logarithmic surface gravity $\log g$ and the iron abundance.

Since the HARPS-N data were collected during transit events for measuring the RM effect, we do not have new out-of-transit RV points for redetermining the velocity amplitude, K_{\star} , of the RV curves. Therefore, we adopted the values from the literature; they are reported in Tables D.1, D.2, D.3, D.4 and D.5, together with the other relevant parameters.

With these input parameters, as in Mancini et al. (2018), we made use of the `JKTABSDIM` code (Southworth et al. 2009) to make new estimates of the main physical properties of the planetary systems HAT-P-17, HAT-P-21, HAT-P-26 and HAT-P-29. By iteratively modifying the velocity amplitude of the planet, `JKTABSDIM` maximizes the agreement between the measured T_{eff} and R_{\star}/a and with those predicted by a set of five theoretical models. A wide range of possible ages for each of the host stars was considered. The code returned five different estimates for each of the output parameters, one for each set of theoretical models, and we took the unweighted means as the final values of the parameters. The corresponding systematic uncertainties, caused by the use of theoretical models, were calculated considering the maximum deviation between the values of the final parameters and the single ones coming from the five theoretical models. Instead, statistical uncertainties were propagated from the error bars in the values of the input parameters. The final values are reported in Tables D.2, D.3, D.4 and D.5, together with values taken from the literature, which are shown there for comparison purposes. Our estimations of the radii and masses for the stars and planets are all within the error bars of literature determinations, but slightly more precise.

10. Discussion

10.1. On the spin-orbit alignment of hot Jupiters

At present (February 2022), TEPcat lists determinations of λ for roughly 170 transiting exoplanets, while ψ has been constrained for only 39. Most of them are hot Jupiters, which represents the only class for which we have a good statistical sample. What can be deduced from this collection of λ measurements for hot Jupiters is a matter of debate. So far, no convincing correlations have emerged from plotting the projected obliquity versus other parameters, such as planetary radius and mass, orbital separation, stellar age, etc. Early studies (e.g., Winn et al. 2010; Albrecht et al. 2012; Dawson 2014; Tregloan-Reed et al. 2015), which were based on a smaller sample of λ measurements, have tentatively identified two populations of more or less aligned hot Jupiters based on the effective temperature of their parent stars. Considering our new data and those listed in TEPcat, we plotted the absolute values of λ of hot Jupiters ($0.3 M_{\text{Jup}} < M_{\text{p}} < 13 M_{\text{Jup}}$ and $a/R_{\star} < 25$) versus T_{eff} in Fig. 9. Of the more than 130 planets appearing in the diagram, only 14 have an eccentricity $e > 0.1$; four of them are the planets presented in this study.

The separation line between the two groups is related to the Kraft break (the remarkable decrease in the rotation velocities observed in main-sequence stars later than F5, Kraft 1967), and falls somewhere between 6090 and 6300 K (see the gray zone in

Fig. 9); planets orbiting stars with mostly convective (radiative) outer envelopes are on the left (right) side of this plot.

Cooler than radiative stars, the convective stars are supposed to have a rapid tidal dissipation as the convective cells produce the turbulent cascades that lead to energy loss. Instead, the radiative stars are thought to have much weaker tidal dissipation. Consequently, the orbit of hot Jupiters hosted by relatively cool stars ($T_{\text{eff}} < 6100$ K) should be much more aligned with the spin of their hosts because tides limit possible obliquity on timescales much shorter than those related to the orbital decay of hot Jupiters. Specifically, the tidal modes responsible for the damping of the obliquity may be different from those producing the orbital decay and can act on a remarkably shorter timescale producing a spin-orbit alignment without a significant decrease of the orbital semi-major axis (Lai 2012; Valsecchi & Rasio 2014; Lanza 2022). As we can see from Fig. 9, although high-obliquity hot Jupiters were found regularly above the Kraft break, there are several exceptions that challenge this theory.

In order to have a more general picture of the current situation, we refer the reader to the top panel of Fig. 10, where we made a polar plot of the measured sky-projected obliquities of all known systems hosting a planet with $M_p < 13 M_{\text{Jup}}$ and a scaled orbital distance a/R_* from the host star up to 25. Even for systems hosting smaller planets, it is difficult to see a correlation between λ and T_{eff} .

Based on the expectations for the rotation velocities of stars with effective temperatures between 5900 and 6600 K from Louden et al. (2021), Albrecht et al. (2021) calculated the expected ψ for a sample of 57 planetary systems. They found that perpendicular orbits ($\psi = 80^\circ - 125^\circ$) are statistically favoured.

According to TEPcat, there are now 25 exoplanets for which we know their radius and have the measurement of ψ . They are shown in another polar plot (bottom panel of Fig. 10), in which most of the exoplanets orbiting cool stars have $\psi < 30^\circ$, whereas the four exoplanets orbiting hot stars ($T_{\text{eff}} \geq 7650$ K) have $60^\circ < \psi < 135^\circ$. However, since the statistical sample is not yet significant, it is hard to make strong assertions.

10.2. Tidal-alignment timescales for the five systems of our study

An estimate of the tidal-alignment timescales in the specific cases of our four systems (HAT-P-15, HAT-P-17, HAT-P-21, and HAT-P-29), based on an adapted version of the tidal model of Leconte et al. (2010) already used in our previous investigations (e.g., Esposito et al. 2017), shows that only HAT-P-21 has an e-folding timescale for the damping of its obliquity of ~ 0.3 Gyr, shorter than the main-sequence lifetime of the star, when we adopt a stellar modified tidal quality factor $Q'_s = 10^6$, as expected for an efficient dissipation of the obliquity tides as in the model by Lai (2012). The age estimated from the observed rotation period of HAT-P-21 using gyrochronology, that is $\sim 1.5 - 2.0$ Gyr, is in tension with the age estimated from the isochrone fitting ($\sim 7.8 \pm 2.6$ Gyr). Its relatively fast rotation could be due to the tides produced by the close-by massive planet that tend to spin-up HAT-P-21 with a characteristic e-folding timescale of ~ 4 Gyr, if we assume a stellar modified tidal quality factor $Q'_s = 10^7$ as suggested, for example, by Jackson et al. (2009). The e-folding timescale for the damping of the orbital eccentricity is ~ 3.3 Gyr, when we adopt modified tidal quality factors $Q'_s = 10^7$ for the star and $Q'_p = 10^7$ for the planet, respectively. The modified tidal quality factor of the planet is obtained by scaling the value of Jupiter to the slow rotation of HAT-P-21 b assumed to be synchronized with its orbital motion (cf. Ogilvie

2014). These considerations suggest that HAT-P-21 is indeed an old star and that the planet could have migrated close to its host through an orbit of initially high eccentricity that was significantly reduced by tides during the main-sequence lifetime of the system together with any initially large obliquity.

Considering the other systems, their orbits also show a significant eccentricity. Assuming $Q'_s = 10^7$ and $Q'_p = 10^7$ as in the case of HAT-P-21 and HAT-P-21b, respectively, the e-folding timescale for the damping of the eccentricity, τ_e , is comparable with the estimated age of the system only in the case of HAT-P-26 ($\tau_e \sim 6$ Gyr), while it is longer for the other systems. The rotation of the hosts and the obliquity of the planetary orbits were not significantly affected by the tides during their main-sequence evolution, even assuming a strong interaction with $Q'_s = 10^6$. In conclusion, these considerations suggest that, with the possible exception of HAT-P-21, the rather small spin-orbit misalignments observed in the other systems are likely to be primordial as well as their significant eccentricities. The only possible exception could be the eccentricity of HAT-P-26, which might require an excitation by a third body to account for the observed values.

11. Summary

Within the GAPS programme, we are observing a sample of transiting-exoplanet systems, mostly hosting hot Jupiters, with the HARPS-N spectrograph, supported by an array of medium-class telescopes. The aim is to better characterize these planetary systems and get information about the degree of orbital alignment of this class of planets, according to the characteristics of their parent stars.

We divided in two groups the five targets under study in this work. In the first group there are four hot Jupiters (HAT-P-15, HAT-P-17, HAT-P-21, and HAT-P-29), while in the second group there is one Neptune-mass planet (HAT-P-26). Details of our new observations are reported in Tables 1 and B.1. Thanks to new spectroscopic and photometric observations that we collected, and the public data from TESS and *Gaia*, we were able to (i) review their physical and orbital parameters and (ii) reveal the RM effect, during transit events, and measure the spin-orbit alignment of these systems.

Our main results are as follows.

- We revised most of the physical parameters of the five planetary systems. Our results are reported in Tables D.1, D.2, D.3, D.4 and D.5, and are in good agreement (and, in general, slightly more accurate) with those obtained previously by other authors.
- We estimated new mid-transit times for four of the systems (HAT-P-17, HAT-P-21, HAT-P-26, and HAT-P-29) and augmented them with published values to obtain lists of transit times. They are reported in Tables C.1, C.2, C.3 and C.4. They were used for updating the orbital periods and expected mid-transit times of the systems. We also searched for evidence of TTVs. Our analysis shows an indication of possible TTVs in the HAT-P-29 planetary system, which must be verified with more data. We determined a new linear ephemeris with an orbital period 17 ± 4.2 s longer than that found by Buchhave et al. (2011). We also confirmed the much stronger indication of TTVs that was found by von Essen et al. (2019) for the HAT-P-26 system. This sinusoidal variation may be caused by a third body in the system. More follow-up observations are required to confirm its existence.

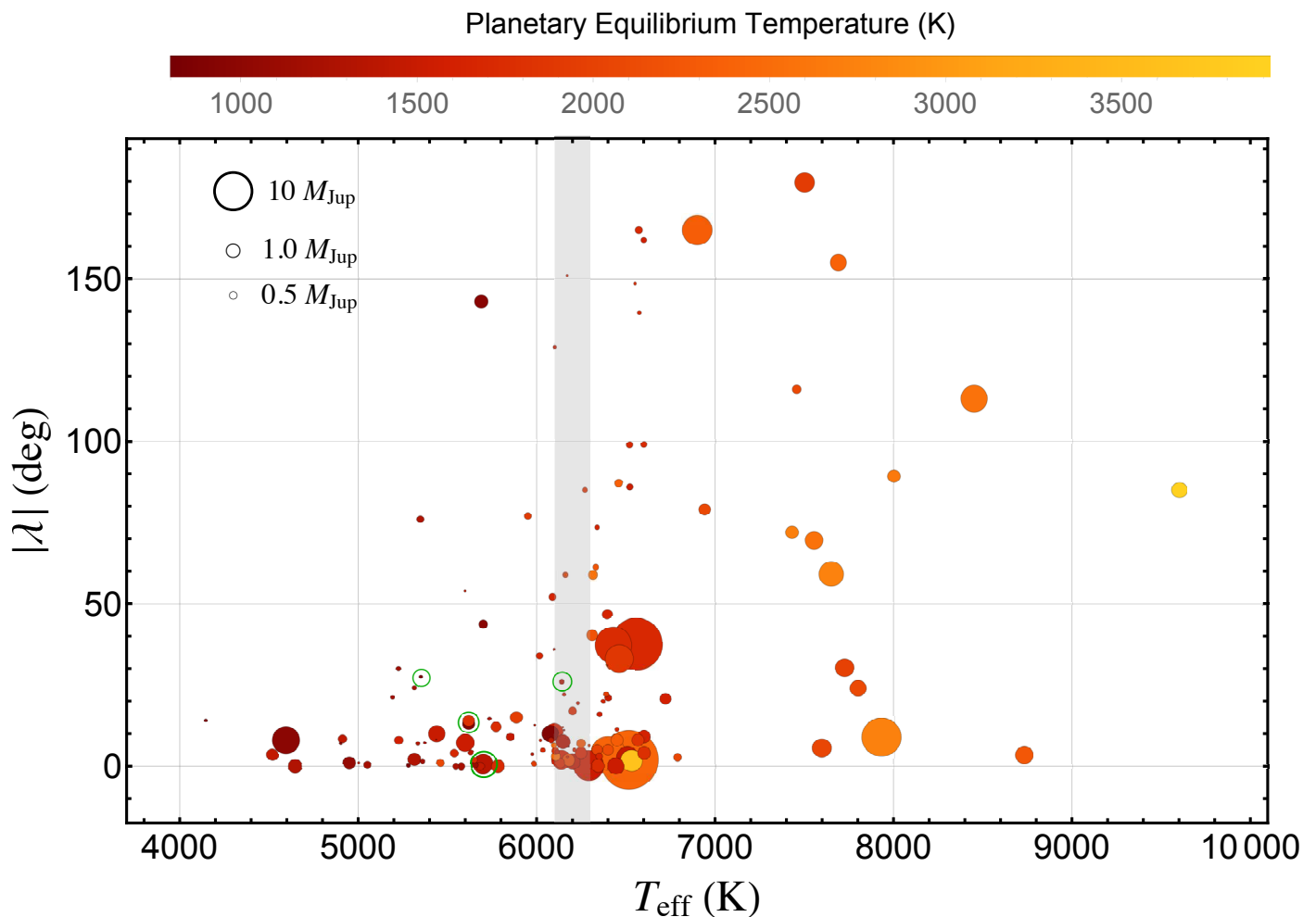


Fig. 9. Absolute values of the sky-projected orbital obliquity angles of close-in exoplanets (with mass $0.3 M_{\text{Jup}} < M_p < 13 M_{\text{Jup}}$ and $a/R_\star < 25$), as a function of the host star's effective temperature. The planets are represented by circles, whose sizes is proportional to their mass. The error bars have been suppressed for clarity. Colour indicates their equilibrium temperature. The grey zone should discriminate two different populations of hot Jupiters, according to several authors (e.g., Winn et al. 2010; Albrecht et al. 2012). The planets surrounded by the green circles are those examined in this work, except for HAT-P-26 b. The other data were taken from TEPcat in February 2022.

- The frequency analysis of the HATNet photometric time-series for HAT-P-21 highlighted a modulation caused by stellar activity, allowing us to get a measurement of the rotational period of the star of $P_{\text{rot}} = 15.88 \pm 0.02$ d. A similar analysis, performed for the HATNet light curves of the other four stars, did not unearth out any clear photometric modulation.
- We used the HARPS-N spectrograph to monitor one transit for each of the five planets. The RM effect was completely covered for HAT-P-15, HAT-P-17, HAT-P-21, HAT-P-29 and only partially for HAT-P-26, which also suffered from adverse weather conditions at the end of the observations. We successfully measured the sky-projected orbital obliquity for four of the systems, obtaining $\lambda = 13^\circ \pm 6^\circ$, $\lambda = -26.3^\circ \pm 6.7^\circ$, $\lambda = -0.7^\circ \pm 12.5^\circ$, $\lambda = -26^\circ \pm 16^\circ$, for HAT-P-15 b, HAT-P-17 b, HAT-P-21 b and HAT-P-29 b, respectively, all indicating good spin-orbit alignments within the uncertainties. Even though we were not able to constrain λ for HAT-P-26 b, the modelling of the data returns a value, $\lambda = 18^\circ \pm 49^\circ$, that also suggests a prograde orbit for this planet; this is also supported by the shape of the RM effect, see Fig. 4. Finally, for the HAT-P-21 system, we were able to determine its true obliquity, obtaining $\psi = 25^\circ \pm 16^\circ$.

We also discuss the case that the sky projected spin-orbit misalignment of exoplanets, especially hot Jupiters, can be correlated with the temperature of their parent stars. We confirm that hot Jupiters with low-obliquity are regularly found orbiting convective stars, with effective temperature below the Kraft break, which have a rapid tidal dissipation when compared with radiative stars. However, the existence of several exceptions makes things not so clear. A further effort to enlarge the sample is required in order to shed new light on the matter.

Finally, we roughly estimated the tidal-alignment timescales of the systems under study and made some deductions about the origin of their rather small spin-orbit misalignments that we measured.

Acknowledgements. This paper is based on observations collected with the following telescopes: the 3.58 m Telescopio Nazionale Galileo (TNG), operated on the island of La Palma (Spain) by the Fundación Galileo Galilei of the INAF (Istituto Nazionale di Astrofisica) at the Spanish Observatorio del Roque de los Muchachos, in the frame of the programme Global Architecture of Planetary Systems (GAPS); the Zeiss 1.23 m telescope at the Centro Astronómico Hispano Alemán (CAHA) in Calar Alto (Spain); the Cassini 1.52 m telescope at the Astrophysics and Space Science Observatory of Bologna in Loiano (Italy); the Copernico telescope (Asiago, Italy) of the INAF - Osservatorio Astronomico di Padova; the 0.82 m IAC 80 Telescope, operated on the island of Tenerife by the Instituto de Astrofísica de Canarias in the Spanish Observatorio del Teide. The HARPS-N instrument has been built by

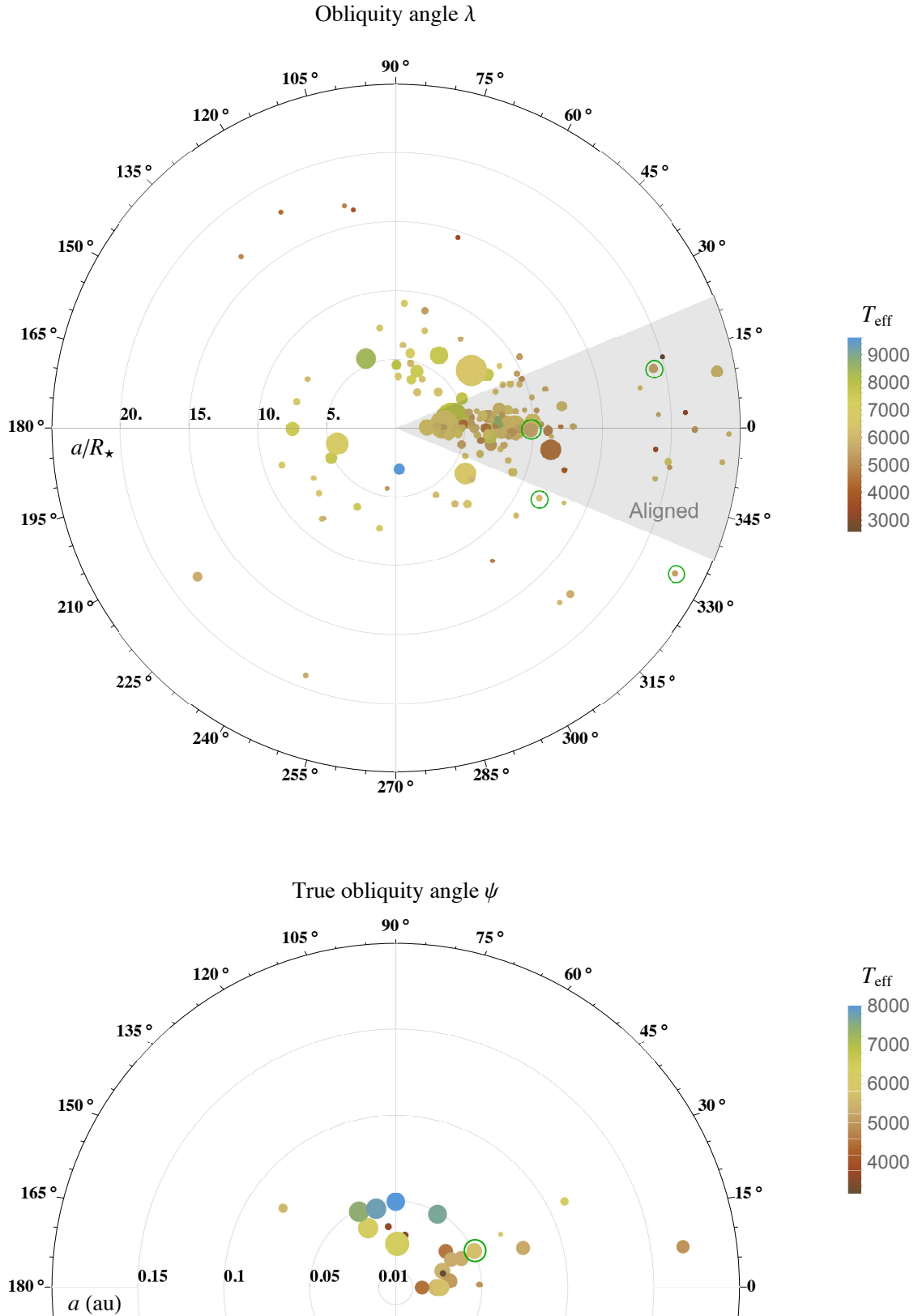


Fig. 10. Top panel: Sky-projected orbital obliquity of known exoplanets as a function of their scaled orbital distance a/R_* from the host star. The plot includes all planets with $M_p < 13 M_{\text{Jup}}$ and $a/R_* < 25$. They are represented by circles, whose sizes is proportional to their mass. The planets surrounded by the green circles are those examined in this work, except for HAT-P-26 b. **Bottom panel:** True orbital obliquity of known exoplanets. They are represented by circles, whose size is proportional to their radius. The planet surrounded by the green circle is HAT-P-21 b, which was examined in this work. **Both panels:** The error bars have been suppressed for clarity. Colour indicates the effective temperature of their parent stars. The data were taken from TEPCat in February 2022. Figure inspired by similar plots from J. Winn; see also Zhou et al. (2019).

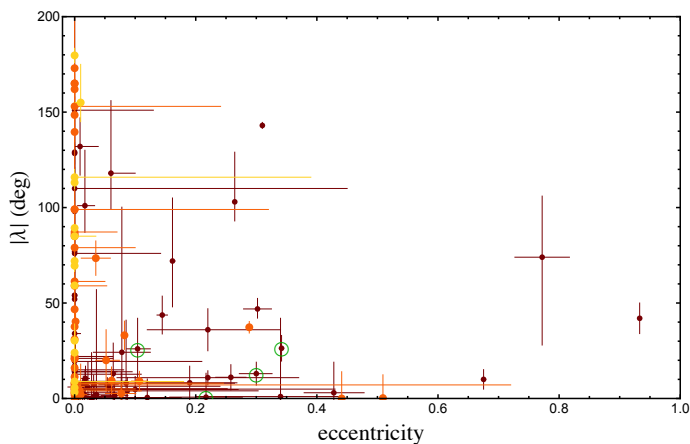


Fig. 11. Sky-projected orbital obliquity of known exoplanets as a function of their orbital eccentricity. Different colours indicate a different value of T_{eff} : dark red are for cool hosts ($T_{\text{eff}} < 6250$ K); orange are for hot hosts $6250 < T_{\text{eff}} < 7000$ K; yellow are for very hot hosts $T_{\text{eff}} > 7000$ K. Many of the planet with eccentricity equal to zero does not have horizontal error bars. The planets surrounded by the green circles are those examined in this work, except for HAT-P-26 b. The other data were taken from TEPcat in February 2022

the HARPS-N Consortium, a collaboration between the Geneva Observatory (PI Institute), the Harvard-Smithsonian Center for Astrophysics, the University of St. Andrews, the University of Edinburgh, the Queen's University of Belfast, and INAF. This research made use of Lightkurve, a Python package for Kepler and TESS data analysis (Lightkurve Collaboration, 2018). The other reduced light curves presented in this work will be made available at the CDS (<http://cdsweb.u-strasbg.fr/>). This work has made use of data from the European Space Agency (ESA) mission *Gaia* (<https://www.cosmos.esa.int/gaia>), processed by the *Gaia* Data Processing and Analysis Consortium (DPAC, <https://www.cosmos.esa.int/web/gaia/dpac/consortium>). Funding for the DPAC has been provided by national institutions, in particular the institutions participating in the *Gaia* Multilateral Agreement. We thank Roberto Gualandri for his technical assistance at the Cassini telescope. We thank the support astronomers of CAHA for their technical assistance at the Zeiss telescope. L.M. acknowledges support from the “Fondi di Ricerca Scientifica d’Ateneo 2021” of the University of Rome “Tor Vergata”. We acknowledge the use of the following internet-based resources: the ESO Digitized Sky Survey; the TEPcat catalogue; the SIMBAD database operated at CDS, Strasbourg, France; and the arXiv scientific paper preprint service operated by Cornell University. ME acknowledges the support of the DFG priority program SPP 992 “Exploring the Diversity of Extrasolar Planets” (HA 3279/12-1).

References

Adams, E. R., Dupree, A. K., Kulesa, C., & McCarthy, D. 2013, *AJ*, 146, 9
 Agol, E., Steffen, J., Sari, R., et al. 2005, *MNRAS*, 359, 567
 Albrecht, S. H., Winn, J. N., Johnson, J. A., et al. 2012, *ApJ*, 757, 18
 Albrecht, S. H., Marcussen, M. L., Winn, J. N., et al. 2021, *ApJ*, 916, L1
 Albrecht, S. H., Dawson, R. I., Winn, J. N. 2022, arXiv:2203.05460
 Bakos, G. Á., Hartman, J. D., Torres, G., et al. 2011, *ApJ*, 742, 116
 Baranne, A., Queloz, D., Mayor, M., et al. 1996, *A&AS*, 119, 373
 Barbato, D., Sozzetti, A., Biazzo, K., et al. 2019, *A&A*, 621, A110
 Belokurov, V., Penoyre, Z., Oh, S., et al. 2020, *MNRAS*, 496, 1922
 Biazzo, K., Gratton, R., Desidera, S., et al. 2015, *A&A*, 583, A135
 Bonomo, A. S., Desidera, S., Benatti, S., et al. 2017, *A&A*, 602, A107
 Buchhave, L. A., Bakos, G. Á., Hartman, J. D., et al. 2011, *ApJ*, 733, 116
 Castelli, F., & Kurucz, R. L. 2003, in *Modelling of Stellar Atmospheres*, N. Piskunov, W. W. Weiss, D. F. Gray (eds.), Published on behalf of the IAU by the Astronomical Society of the Pacific, p. A20
 Chatterjee, S., Ford, E. B., Matsumura, S., Rasio, F. A. 2008, *ApJ*, 686, 580
 Choi, J., Dotter, A., Conroy, C., et al. 2016, *ApJ*, 823, 102
 Ciceri, S., Mancini, L., Southworth, J., et al. 2013, *A&A*, 557, A30
 Cochran, W. D., Hatzes, A. P., Butler, R. P., Marcy, G. W. 1997, *ApJ*, 483, 457
 Cosentino, R., Lovis, C., Pepe, F., et al. 2012, in *Proc. SPIE*, 8446, 1
 Cosentino, R., Lovis, C., Pepe, F., et al. 2014, in *Proc. SPIE*, 9147, 8
 Covino, E., Esposito, M., Barbieri, M., et al. 2013, *A&A*, 554, A28
 Damasso, M., Biazzo, K., Bonomo, A. S., et al. 2015, *A&A*, 575, 111

Davies, M. B., Adams, F. C., Armitage, P., et al. 2014, in *Protostars and Planets VI*, Henrik Beuther, Ralf S. Klessen, Cornelis P. Dullemond, and Thomas Henning (eds.), University of Arizona Press, Tucson, p. 787
 Dawson, R. I., Murray-Clay, R. A., 2013, *ApJ*, 767, L24
 Dawson, R. I. 2014, *ApJ*, 790, 31
 Dotter, A. 2016, *ApJS*, 222, 8
 Dravins, D., Nordlund, A. 1990, *A&A*, 228, 184
 Eastman, J. D., Rodriguez, J. E., Agol, E., et al. 2019, arXiv:1907.09480
 Esposito, M., Covino, E., Mancini, L., et al. 2014, *A&A*, 564, L13
 Esposito, M., Covino, E., Desidera, S., et al. 2017, *A&A*, 601, A53
 Fulton, B. J., Howard, A. W., Winn, J. N., et al. 2013, *ApJ*, 772, 80
 Gaia Collaboration, Prusti, T., de Bruijne, J. H. J., et al. 2016, *A&A*, 595,
 Gaia Collaboration, Brown, A. G. A., Vallenari, A., et al. 2021, *A&A*, 649, A1
 Gibson, N. P., Pollacco, D., Simpson, E. K., et al., 2009, *ApJ*, 700, 1078
 Hartman, J., Bakos, G. Á., Kipping, D. M., et al. 2011, *ApJ*, 728, 138
 Howard, A. W., Bakos, G. Á., Hartman, J., et al. 2012, *ApJ*, 749, 134
 Jackson, B., Barnes, R., Greenberg, R. 2009, *ApJ*, 698, 1357
 Kipping, D. M. 2008, *MNRAS*, 389, 1383
 Knutson, H. A., Fulton, B. J., Montet, B. T., et al. 2014, *ApJ*, 785, 126
 Kovács, G., Bakos, G. Á., Noyes, R. W. 2005, *MNRAS*, 356, 557
 Kovács, G., Bakos, G. Á., Hartman, J. D., et al. 2010, *ApJ*, 724, 866
 Kraft, R. P. 1967, *ApJ*, 150, 551
 Lai, D. 2012, *MNRAS*, 423, 486
 Lanza, A. F. 2020, *MNRAS*, 497, 3911
 Lanza, A. F. 2022, *A&A*, 658, A195
 Lecointe, J., Chabrier, G., Baraffe, I., et al. 2010, *A&A*, 516, A64
 Lin, D. N. C., Bodenheimer, P., Richardson, D. C. 1996, *Nature*, 380, 606
 Louden, E. M., Winn, J. N., Petigura, E. A., et al. 2021, *AJ*, 161, 68
 Lovis, C., & Pepe, F. 2007, *A&A*, 468, 1115
 Lovis, C., Dumusque, X., Santos, N. C., et al. 2011, arXiv:1107.5325
 MacDonald, R. J. & Madhusudhan, N. 2019, *MNRAS*, 486, 192
 Mayor, M., Queloz, D. 1995, *Nature*, 378, 355
 Mallonn, M., von Essen, C., Herrero, E., et al. 2019, *A&A*, 622, A81
 Mancini, L., Southworth, J., Ciceri, S., et al. 2013, *A&A*, 551, A11
 Mancini, L., Esposito, M., Covino, E., et al. 2015, *A&A*, 579, A136
 Mancini, L., Southworth, J., Raia, G., et al. 2017, *MNRAS*, 465, 843
 Mancini, L., Esposito, M., Covino, E., et al. 2018, *A&A*, 613, A41
 Marzari, F., Nelson, A. F. 2009, *ApJ*, 705, 1575
 Mortier, A., Santos, N. C., Sousa, S. G., et al. 2013, *A&A*, 558, A106
 Matsumura, S., Peale, S. J., Rasio, F. A. 2010, *ApJ*, 725, 1995
 Nascimbeni, V., Piotto, G., Bedin, L. R., Damasso, M. 2011, *A&A*, 527, A85
 Ngo, H., Knutson, H. A., Hinkley, S., et al., 2015, *ApJ*, 800, 138
 Ngo, H., Knutson, H. A., Hinkley, S., et al., 2016, *ApJ*, 827, 8
 Ogilvie, G. I. 2014, *ARA&A*, 52, 171
 Pepe, F., Mayor, M., Galland, F., et al. 2002, *A&A*, 388, 632
 Piskorz, D., Knutson, H. A., Ngo, H., et al. 2015, *ApJ*, 814, 148
 Rasio, F. A., Ford, E. B. 1996, *Science*, 274, 954
 Raymond, S. N., Morbidelli, A. 2022, in *Biazzo K., Bozza V., Mancini L., Sozzetti A. (eds.), Demographics of Exoplanetary Systems. Astrophysics and Space Science Library 466*, Springer International Publishing, Switzerland, p. 3
 Rice, M., Wang, S., Howard, A. W., et al. 2021, *AJ*, 162, 182
 Rice, M., Wang, S., Laughlin, G. 2022, *ApJ*, 926, L17
 Ricker, G. R., Winn, J. N., Vanderspek, R., et al. 2015, *J. Astron. Telesc. Instrum. Syst.*, 1, 014003.
 Shporer, A., Brown, T. M. 2011, *ApJ*, 733, 30
 Smareglia, R., Bignamini, A., Knäpik, C., Molinaro, M., & GAPS Collaboration 2014, in *Astronomical Data Analysis Software and Systems XXIII*, eds. N. Manset, & P. Forshay, ASP Conf. Ser., 485, 435
 Sneden, C. A. 1973, *ApJ*, 184, 839
 Southworth, J., Hinse, T. C., Dominik, M., et al. 2009, *ApJ*, 707, 167
 Southworth J. 2011, *MNRAS*, 417, 2166
 Southworth, J., Bruni, I., Mancini, L., Gregorio, J. 2012, *MNRAS*, 420, 2580
 Southworth, J. 2013, *A&A*, 557, A119
 Southworth, J., Hinse, T. C., Burgdorf, M., et al. 2014, *MNRAS*, 444, 776
 Stassun, K. G., Collins, K. A., Gaudi, B. S. 2017, *AJ*, 153, 136
 Stassun, K. G. & Torres, G. 2018, *ApJ*, 862, 61
 Stevenson, K. B., Bean, J. L., Seifahrt, A., et al. 2016, *ApJ*, 817, 141
 Torres, G., Fischer, D. A., Sozzetti, A., et al. 2012, *ApJ*, 757,
 Tregloan-Reed, J., Southworth, J., Burgdorf, M., et al. 2015, *MNRAS*, 450, 1760
 Valsecchi, F., Rasio, F. A. 2014, *ApJ*, 786, 102
 von Essen, C., Wedemeyer, S., Sosa, M. S., et al. 2019, *A&A*, 628, A116
 Wakeford, H. R., Sing, D. K., Kataria, T., et al. 2017, *Science*, 356, 628
 Wang, S., Wang, X.-Y., Wang, Y.-H., et al. 2018, *AJ*, 156, 181
 Wang, S., Winn, J. N., Addison, B. C., et al. 2021, *AJ*, 162, 50,
 Ward, W. R. 1997, *ApJ*, 482, L211
 Winn, J. N., Holman, M. J., Henry, G. W., et al. 2007, *AJ*, 133, 1828
 Winn, J. N., Fabrycky, D., Albrecht, S., Johnson, J. A. 2010, *ApJ*, 718, L145
 Wöllert, M., Brandner, W., Bergfors, C., & Henning, T. 2015, *A&A*, 575, A23
 Wöllert, M. & Brandner, W. 2015, *A&A*, 579, A129

Wu, Y., Murray, N. 2003, ApJ, 589, 605

Zhou, G., Bakos, G. Á., Bayliss, D., et al. 2019, AJ, 157, 31

-
- ¹ Department of Physics, University of Rome “Tor Vergata”, Via della Ricerca Scientifica 1, 00133 – Rome, Italy
e-mail: lmancini@roma2.infn.it
 - ² Max Planck Institute for Astronomy, Königstuhl 17, 69117 – Heidelberg, Germany
 - ³ INAF – Osservatorio Astrofisico di Torino, via Osservatorio 20, 10025 – Pino Torinese, Italy
 - ⁴ Thüringer Landessternwarte, Tautenburg Sternwarte 5, 07778 – Tautenburg, Germany
 - ⁵ INAF – Osservatorio Astronomico di Capodimonte, Salita Moiarriello 16, 80131 – Naples, Italy
 - ⁶ Astrophysics Group, Keele University, Keele ST5 5BG, UK
 - ⁷ INAF – Osservatorio Astronomico di Brera, Via E. Bianchi 46, 23807 – Merate (LC), Italy
 - ⁸ Fundación Galileo Galilei - INAF, Rambla José Ana Fernández Pérez 7, 38712 Breña Baja, TF, Spain
 - ⁹ INAF – Osservatorio Astronomico di Roma, Via Frascati 33, 00078 – Monte Porzio Catone (Roma), Italy
 - ¹⁰ Observatoire de Genève, Université de Genève, 51 Chemin Pegasi, 1290 – Sauverny, Switzerland
 - ¹¹ INAF – Osservatorio Astronomico di Padova, Vicolo dell’Osservatorio 5, 35122 – Padova, Italy
 - ¹² Dipartimento di Fisica e Astronomia “Galileo Galilei” – Università di Padova, Vicolo dell’Osservatorio 2, 35122 – Padova, Italy
 - ¹³ INAF – OAS, Osservatorio di Astrofisica e Scienza dello Spazio di Bologna, Via P. Gobetti 93/3, 40129 – Bologna, Italy
 - ¹⁴ INAF – Osservatorio Astrofisico di Catania, via S. Sofia 78, 95123 – Catania, Italy
 - ¹⁵ Department of Physics and Astronomy, University of Florence, Largo Enrico Fermi 5, 50125 Firenze
 - ¹⁶ Instituto de Investigación en Astronomía y Ciencias Planetarias, Universidad de Atacama, Copiapó, Atacama, Chile
 - ¹⁷ INAF – Osservatorio Astronomico di Trieste, via Tiepolo 11, 34143 – Trieste, Italy
 - ¹⁸ INAF – Osservatorio Astronomico di Palermo, Piazza del Parlamento, 1, 90134 – Palermo, Italy
 - ¹⁹ INAF – Osservatorio Astronomico di Cagliari, via della Scienza 5, 09047 – Selargius (CA), Italy

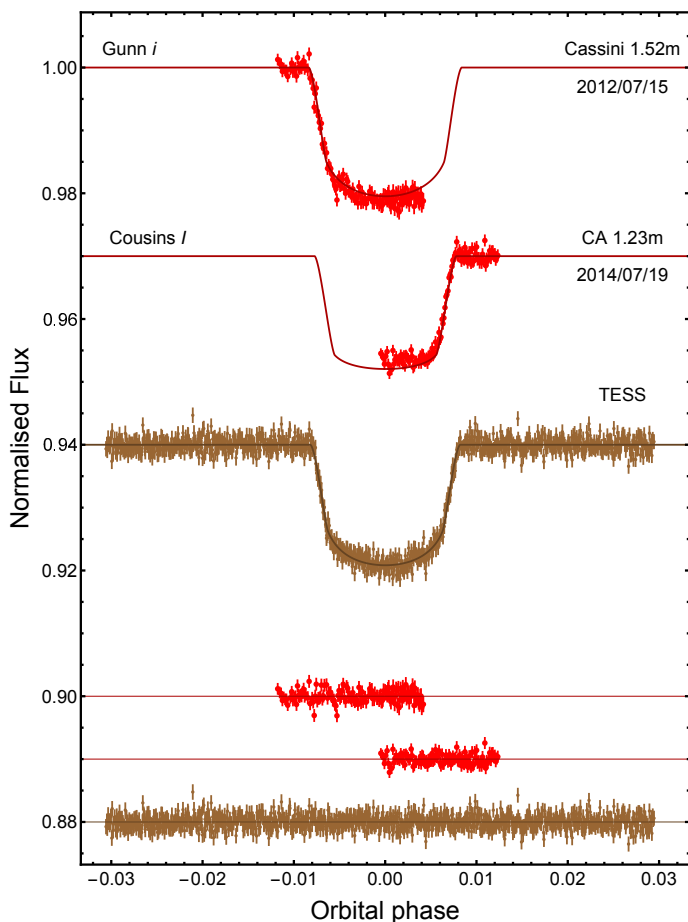


Fig. B.1. Phased light curves of HAT-P-17 b transits presented in this work. Two incomplete transits were observed with ground-based telescopes. Two complete transits were observed with TESS; they are plotted phased. These light curves are compared with the best JKTEBOP fits. The dates, telescopes, and filters related to the observation of each transit event are indicated. Residuals from the fits are plotted at the bottom of the figure.

Appendix A: HARPS-N RV measurements

The RV measurements, which were obtained with HARPS-N (this work), are reported in this appendix.

Appendix B: Photometric light curves

The light curves, which were analysed in this work, are plotted in this appendix. A table with the details of the ground-based photometric follow-up observations is also reported.

Appendix C: Times of mid-transit

The tables in this appendix report the value of the mid-transit times analysed for reviewing the orbital ephemeris of the HAT-P-17, HAT-P-21, HAT-P-26, and HAT-P-29 planetary systems. The figures in this appendix contain the corresponding plots of the residuals of the timings of mid-transit versus a linear ephemeris.

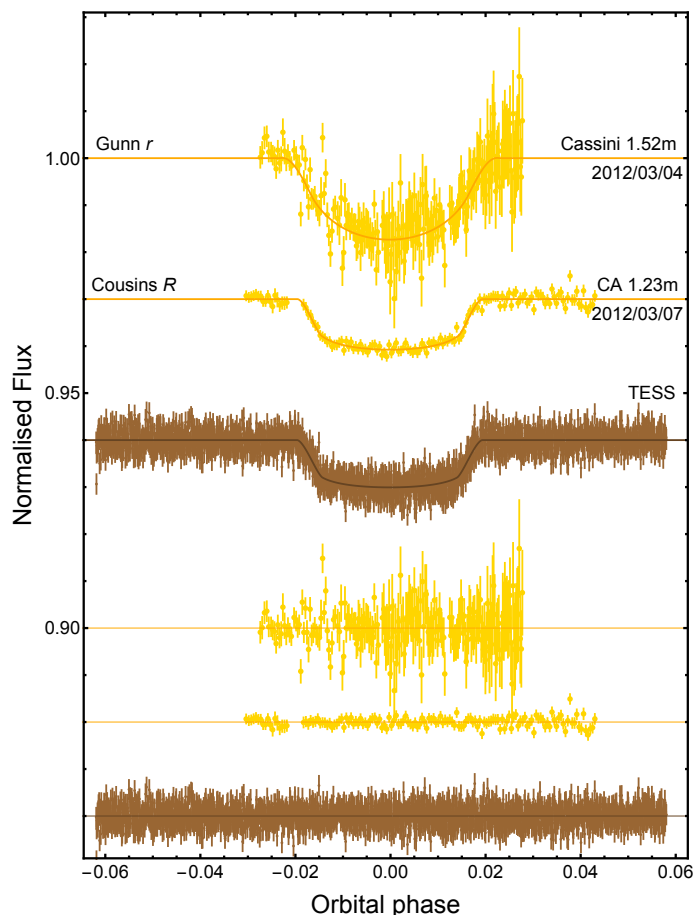


Fig. B.2. Phased light curves of HAT-P-21 b transits presented in this work. Two transits were observed with ground-based telescopes, and five were obtained by TESS. The light curves are compared with the best JKTEBOP fits. The dates, telescopes, and filters related to the observation of each transit event are indicated. Residuals from the fits are plotted at the bottom of the figure.

Appendix D: Revised physical parameters of the planetary systems

The tables in this appendix report the final values that we obtained for the main physical parameters of the planetary systems under study. The values obtained in this work (Sect. 9) are compared with those taken from the literature. Where two error bars are given, the first refers to the statistical uncertainties and the second to the systematic errors.

Table A.1. HARPS-N RV data for HAT-P-15.

BJD (TDB)	T_{exp} [sec]	RV [km s ⁻¹]	error [km s ⁻¹]	FWHM [km s ⁻¹]	Bis. Span [km s ⁻¹]	Airmass	Flag
2 457 343.405902	900	31.7623	0.0040	7.20	-0.018	1.62	o
2 457 343.416435	900	31.7730	0.0041	7.19	-0.025	1.52	o
2 457 343.427373	900	31.7659	0.0040	7.20	-0.012	1.44	o
2 457 343.438021	900	31.7601	0.0034	7.18	-0.031	1.37	o
2 457 343.448820	900	31.7675	0.0034	7.19	-0.015	1.30	i
2 457 343.459318	900	31.7639	0.0034	7.19	-0.036	1.25	i
2 457 343.470117	900	31.7646	0.0042	7.19	-0.030	1.21	i
2 457 343.481032	900	31.7661	0.0042	7.18	-0.032	1.17	i
2 457 343.491564	900	31.7729	0.0032	7.21	-0.017	1.13	i
2 457 343.502213	900	31.7681	0.0033	7.20	-0.027	1.11	i
2 457 343.512827	900	31.7708	0.0034	7.21	-0.021	1.08	i
2 457 343.524991	900	31.7655	0.0038	7.19	-0.021	1.06	i
2 457 343.535397	900	31.7650	0.0037	7.19	-0.018	1.05	i
2 457 343.546381	900	31.7629	0.0034	7.21	-0.010	1.03	i
2 457 343.556798	900	31.7546	0.0033	7.19	-0.023	1.02	i
2 457 343.567423	900	31.7481	0.0035	7.21	-0.017	1.02	i
2 457 343.578222	900	31.7522	0.0037	7.20	-0.010	1.02	i
2 457 343.589160	900	31.7487	0.0036	7.19	-0.014	1.02	i
2 457 343.599773	900	31.7468	0.0032	7.20	-0.033	1.02	i
2 457 343.610468	900	31.7397	0.0030	7.18	-0.025	1.03	i
2 457 343.620955	900	31.7385	0.0030	7.21	-0.027	1.04	i
2 457 343.631846	900	31.7378	0.0032	7.21	-0.008	1.06	i
2 457 343.642668	900	31.7397	0.0031	7.19	-0.028	1.08	i
2 457 343.653513	900	31.7355	0.0030	7.20	-0.028	1.10	i
2 457 343.664069	900	31.7428	0.0027	7.19	-0.020	1.13	i
2 457 343.674741	900	31.7517	0.0027	7.18	-0.024	1.16	i
2 457 343.685401	900	31.7448	0.0027	7.18	-0.025	1.19	o
2 457 343.696188	900	31.7463	0.0028	7.20	-0.016	1.24	o
2 457 343.706906	900	31.7447	0.0027	7.20	-0.025	1.29	o
2 457 343.717450	900	31.7408	0.0030	7.19	-0.008	1.35	o
2 457 343.728029	900	31.7403	0.0035	7.19	-0.023	1.42	o
2 457 343.739465	900	31.7464	0.0034	7.19	-0.026	1.50	o
2 457 343.749986	900	31.7417	0.0036	7.20	-0.024	1.59	o

Notes. The columns report: BJD (TDB), the mid-exposure Barycentric Julian Dates in Barycentric Dynamical Time; T_{exp} , the exposure time; RV and error are the radial velocity measurement and its estimated uncertainty; FWHM, the Full Width at Half Maximum of the Cross-Correlation Function; Bis. Span, the radial velocity bisector span of the CCF; Airmass, the airmass of the star at the beginning of the exposure; Flag, indicating whether the spectrum was taken in-transit (i) or off-transit (o).

Table A.2. HARPS-N RV data for HAT-P-17. Same columns as in Table A.1.

BJD (TDB)	T_{exp} [sec]	RV [km s ⁻¹]	error [km s ⁻¹]	FWHM [km s ⁻¹]	Bis. Span [km s ⁻¹]	Airmass	Flag
2 456 579.321287	900	20.3041	0.0013	6.74	-0.043	1.07	i
2 456 579.333644	900	20.3097	0.0015	6.74	-0.041	1.04	i
2 456 579.344361	900	20.3111	0.0015	6.74	-0.034	1.03	i
2 456 579.355070	900	20.3122	0.0012	6.74	-0.040	1.02	i
2 456 579.365796	900	20.3140	0.0013	6.73	-0.037	1.01	i
2 456 579.375810	900	20.3115	0.0014	6.73	-0.036	1.00	i
2 456 579.387239	900	20.3065	0.0015	6.74	-0.041	1.00	i
2 456 579.397948	900	20.3047	0.0014	6.73	-0.040	1.00	i
2 456 579.408740	900	20.3018	0.0012	6.75	-0.035	1.01	i
2 456 579.419453	900	20.3010	0.0013	6.73	-0.044	1.02	i
2 456 579.430166	900	20.2960	0.0013	6.74	-0.045	1.03	i
2 456 579.440874	900	20.2920	0.0012	6.74	-0.036	1.04	i
2 456 579.451587	900	20.2912	0.0013	6.74	-0.036	1.06	i
2 456 579.462300	900	20.2893	0.0013	6.74	-0.048	1.09	i
2 456 579.473017	900	20.2968	0.0013	6.73	-0.039	1.12	i
2 456 579.483726	900	20.2965	0.0013	6.74	-0.038	1.15	i
2 456 579.494438	900	20.2970	0.0013	6.74	-0.039	1.20	o
2 456 579.505160	900	20.2976	0.0013	6.74	-0.038	1.25	o
2 456 579.515868	900	20.2955	0.0013	6.74	-0.039	1.30	o
2 456 579.526586	900	20.2946	0.0013	6.74	-0.039	1.37	o
2 456 579.537298	900	20.2941	0.0013	6.74	-0.042	1.45	o
2 456 579.548011	900	20.2938	0.0013	6.74	-0.041	1.54	o
2 456 579.560168	900	20.2962	0.0016	6.74	-0.045	1.67	o

Table A.3. HARPS-N RV data for HAT-P-21. Same columns as in Table A.1.

BJD (TDB)	T_{exp} [sec]	RV [km s ⁻¹]	error [km s ⁻¹]	FWHM [km s ⁻¹]	Bis. Span [km s ⁻¹]	Airmass	Flag
2456724.442357	600	-52.8637	0.0064	8.21	0.021	1.28	o
2456724.449582	600	-52.8660	0.0063	8.26	0.002	1.24	o
2456724.456804	600	-52.8727	0.0060	8.20	0.043	1.21	o
2456724.464026	600	-52.8741	0.0057	8.21	0.025	1.19	o
2456724.471252	600	-52.8720	0.0060	8.22	0.017	1.16	o
2456724.478478	600	-52.8810	0.0069	8.21	0.034	1.14	o
2456724.485705	600	-52.8845	0.0075	8.23	0.042	1.12	o
2456724.492931	600	-52.9000	0.0062	8.21	0.030	1.10	i
2456724.500144	600	-52.8909	0.0063	8.20	0.005	1.09	i
2456724.507366	600	-52.8949	0.0060	8.22	0.030	1.07	i
2456724.514595	600	-52.8935	0.0059	8.21	0.014	1.06	i
2456724.521825	600	-52.8871	0.0062	8.20	0.021	1.05	i
2456724.529047	600	-52.8948	0.0050	8.18	0.020	1.04	i
2456724.536282	600	-52.8960	0.0055	8.20	0.012	1.04	i
2456724.543512	600	-52.9001	0.0069	8.20	0.017	1.03	i
2456724.550742	600	-52.9140	0.0070	8.23	0.010	1.03	i
2456724.557982	600	-52.9195	0.0067	8.23	0.037	1.02	i
2456724.565212	600	-52.9277	0.0053	8.23	0.021	1.02	i
2456724.572433	600	-52.9349	0.0046	8.24	0.016	1.02	i
2456724.579654	600	-52.9463	0.0058	8.22	0.031	1.02	i
2456724.586872	600	-52.9542	0.0095	8.26	0.047	1.03	i
2456724.594098	600	-52.9690	0.0064	8.24	0.016	1.03	i
2456724.601319	600	-52.9625	0.0066	8.23	0.034	1.04	i
2456724.608540	600	-52.9645	0.0061	8.21	0.030	1.05	i
2456724.615766	600	-52.9720	0.0079	8.22	0.037	1.05	i
2456724.622988	600	-52.9893	0.0089	8.17	0.032	1.07	i
2456724.630200	600	-52.9778	0.0433	8.29	0.169	1.08	i
2456724.637426	600	-52.9401	0.0679	8.32	0.186	1.09	i
2456724.644648	600	-52.9836	0.0136	8.23	0.000	1.11	i
2456724.651878	600	-52.9986	0.0158	8.21	0.033	1.13	i
2456724.659090	600	-52.9779	0.0094	8.18	0.024	1.15	i
2456724.666316	600	-52.9999	0.0086	8.19	0.019	1.17	i
2456724.673543	600	-52.9878	0.0068	8.23	0.080	1.20	o
2456724.680770	600	-53.0202	0.0093	8.20	0.058	1.22	o
2456724.687986	600	-53.0051	0.0097	8.20	0.050	1.25	o
2456724.695247	430	-52.9971	0.0411	8.20	0.000	1.28	o

Table A.4. HARPS-N RV data for HAT-P-26. Same columns as in Table A.1.

BJD (TDB)	T_{exp} [sec]	RV [km s^{-1}]	error [km s^{-1}]	FWHM [km s^{-1}]	Bis. Span [km s^{-1}]	Airmass	Flag
2 457 108.501404	600	13.8467	0.0049	6.01	0.007	1.60	i
2 457 108.508661	600	13.8524	0.0059	6.02	0.015	1.53	i
2 457 108.515896	600	13.8539	0.0075	5.99	0.020	1.47	i
2 457 108.523127	600	13.8450	0.0057	6.01	-0.003	1.41	i
2 457 108.530357	600	13.8499	0.0052	6.01	0.000	1.37	i
2 457 108.537592	600	13.8450	0.0045	6.03	-0.004	1.32	i
2 457 108.544827	600	13.8477	0.0045	6.00	-0.015	1.29	i
2 457 108.552079	600	13.8400	0.0063	6.00	0.016	1.25	i
2 457 108.559314	600	13.8453	0.0072	5.98	0.011	1.23	i
2 457 108.566541	600	13.8462	0.0070	6.02	0.016	1.20	i
2 457 108.573780	600	13.8351	0.0070	5.98	0.001	1.18	i
2 457 108.581010	600	13.8419	0.0069	6.00	0.019	1.16	i
2 457 108.588255	600	13.8465	0.0056	6.00	-0.018	1.14	i
2 457 108.595494	600	13.8408	0.0049	6.02	0.001	1.13	i
2 457 108.602729	600	13.8487	0.0048	6.00	-0.003	1.12	i
2 457 108.609973	600	13.8466	0.0050	6.00	0.008	1.11	i
2 457 108.617212	600	13.8386	0.0048	6.00	-0.010	1.11	o
2 457 108.624457	600	13.8432	0.0050	5.99	-0.001	1.10	o
2 457 108.631683	600	13.8432	0.0048	6.01	0.023	1.10	o
2 457 108.638927	600	13.8476	0.0062	6.01	-0.010	1.10	o
2 457 108.646180	600	13.8526	0.0060	6.02	0.017	1.10	o
2 457 108.653455	600	13.8406	0.0090	5.98	-0.010	1.11	o
2 457 108.660704	600	13.8463	0.0139	5.97	0.024	1.12	o
2 457 108.667931	600	13.8507	0.0129	6.00	0.009	1.13	o
2 457 108.675161	600	13.8481	0.0281	6.01	-0.028	1.14	o
2 457 108.682391	600	13.8284	0.0170	5.98	-0.004	1.16	o
2 457 108.689625	600	13.8211	0.0202	6.04	-0.073	1.17	o

Table A.5. HARPS-N RV data for HAT-P-29. Same columns as in Table A.1.

BJD (TDB)	T_{exp} [sec]	RV [km s^{-1}]	error [km s^{-1}]	FWHM [km s^{-1}]	Bis. Span [km s^{-1}]	Airmass	Flag
2 456 582.520463	900	-21.6462	0.0054	9.14	0.032	1.12	o
2 456 582.532879	900	-21.6450	0.0053	9.17	0.033	1.10	o
2 456 582.543602	900	-21.6329	0.0056	9.17	0.034	1.10	o
2 456 582.554320	900	-21.6450	0.0056	9.15	0.030	1.09	i
2 456 582.565039	900	-21.6208	0.0055	9.10	0.040	1.09	i
2 456 582.575761	900	-21.6168	0.0051	9.15	0.025	1.09	i
2 456 582.586475	900	-21.6169	0.0045	9.11	0.027	1.09	i
2 456 582.597193	900	-21.6130	0.0047	9.14	0.015	1.09	i
2 456 582.607902	900	-21.6223	0.0048	9.16	0.037	1.10	i
2 456 582.618616	900	-21.6420	0.0048	9.18	0.025	1.12	i
2 456 582.629330	900	-21.6328	0.0050	9.17	0.022	1.13	i
2 456 582.640048	900	-21.6488	0.0052	9.17	0.047	1.15	i
2 456 582.650837	900	-21.6642	0.0071	9.17	0.032	1.17	i
2 456 582.661551	900	-21.6795	0.0078	9.16	0.017	1.20	i
2 456 582.672260	900	-21.6765	0.0123	9.12	0.033	1.23	i
2 456 582.682983	900	-21.6745	0.0082	9.11	0.005	1.26	i
2 456 582.693692	900	-21.6841	0.0060	9.11	0.024	1.30	i
2 456 582.704406	900	-21.6777	0.0054	9.13	0.026	1.35	i
2 456 582.715119	900	-21.6559	0.0052	9.13	0.023	1.40	i
2 456 582.725833	900	-21.6533	0.0057	9.14	0.046	1.46	o
2 456 582.736547	900	-21.6594	0.0062	9.17	0.042	1.53	o
2 456 582.747265	900	-21.6641	0.0067	9.15	0.002	1.61	o
2 456 582.759854	900	-21.6700	0.0072	9.17	0.053	1.72	o

Table B.1. Details of the photometric follow-up observations presented in this work.

Telescope	Date of first obs	Start time (UT)	End time (UT)	N_{obs}	T_{exp} (s)	Filter	Scatter (mmag)
HAT-P-17:							
Cassini 1.52 m	2012.07.15	21:11	01:08	146	60 – 120	Gunn <i>i</i>	0.93
CA 1.23 m	2014.07.20	00:55	04:05	117	60 – 100	Cousins <i>I</i>	0.79
HAT-P-21:							
Cassini 1.52 m	2012.03.03	21:54	00:47	211	60	Gunn <i>r</i>	4.23
CA 1.23 m	2012.03.07	00:55	05:10	145	110 – 120	Cousins <i>I</i>	0.99
HAT-P-26:							
CA 1.23 m	2012.03.04	01:21	05:50	67	120	Cousins <i>I</i>	0.69
CA 1.23 m	2014.04.17	21:54	04:40	209	90 – 120	Cousins <i>I</i>	0.75
CA 1.23 m	2016.03.14	22:14	03:07	190	110	Cousins <i>I</i>	1.01
CA 1.23 m	2017.04.22	20:52	04:08	171	120	Cousins <i>I</i>	1.70
CA 1.23 m	2018.02.26	00:23	06:06	282	45 – 100	Cousins <i>I</i>	0.95
HAT-P-29:							
CA 1.23 m	2011.10.03	22:13	05:07	121	120	Cousins <i>R</i>	0.58
TNG 3.58 m	2012.10.10	01:05	05:25	783	15	Johnson <i>R</i>	0.33
CA 1.23 m	2012.11.01	20:37	04:12	180	105 – 180	Cousins <i>R</i>	1.18
IAC 80 cm	2013.10.16	23:21	04:53	234	60	Cousins <i>R</i>	1.01
Copernico 1.80 m	2014.10.29	17:54	00:02	2303	7	Sloan <i>r</i>	0.67
Copernico 1.80 m	2016.01.07	17:20	23:26	2062	7	Sloan <i>r</i>	0.54
CA 1.23 m	2014.10.23	21:52	05:19	254	95 – 120	Cousins <i>I</i>	0.58
CA 1.23 m	2020.10.23	21:04	05:40	564	30 – 70	Cousins <i>I</i>	0.95

Notes. N_{obs} is the number of observations, T_{exp} is the exposure time. Scatter is the *rms* scatter of the data versus a fitted model.

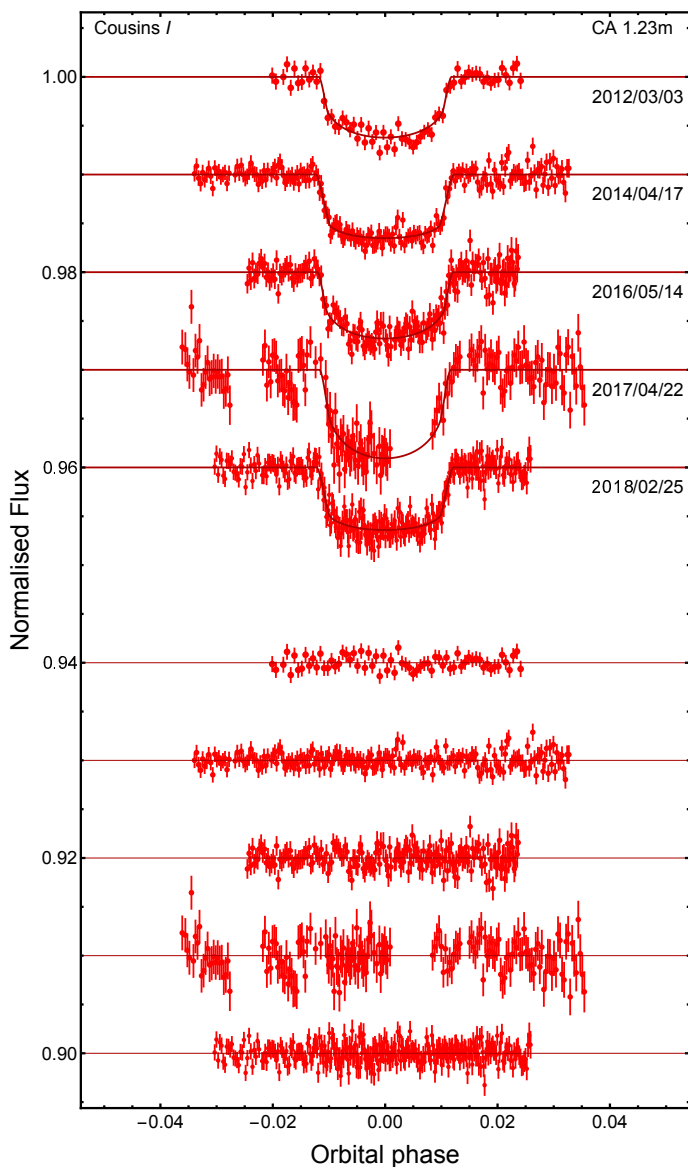


Fig. B.3. Phased light curves of HAT-P-26 b transits presented in this work. Five transits were observed with the CA 1.23 m telescope. These phased light curves are compared with the best χ^2 fits. The dates, telescopes, and filters related to the observation of each transit event are indicated. Residuals from the fits are plotted at the bottom of the figure.

Table C.1. Times of mid-transit for HAT-P-17 b and their residuals for a constant period ($P_{\text{orb}} = 10.33853781 \pm 0.00000060$).

Time of minimum BJD(TDB)–2 400 000	Cycle no.	O – C (day)	Reference
54 801.16943 \pm 0.00020	0	–0.000002	Howard et al. (2012)
56 124.50251 \pm 0.00055	128	0.000239	Cassini (this work)
56 858.53815 \pm 0.00055	199	–0.000306	CA (this work)
58 719.47555 \pm 0.00031	379	0.000289	TESS (this work)
58 729.81360 \pm 0.00027	380	–0.000199	TESS (this work)

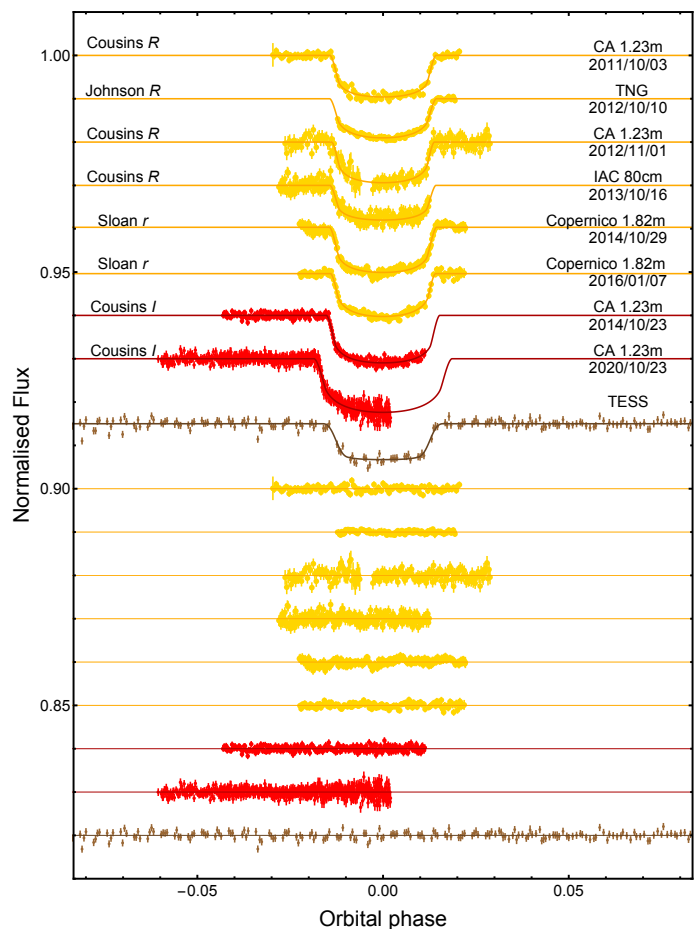


Fig. B.4. Phased light curves of HAT-P-29 b transits presented in this work. Two transits were observed with ground-based telescopes. Other four with TESS; they are plotted phased. The light curves obtained with the Copernico and the TNG telescopes have been also binned. All the light curves are compared with the best χ^2 fits. The dates, telescopes, and filters related to the observation of each transit event are indicated. Residuals from the fits are plotted at the bottom of the figure.

Table C.2. Times of mid-transit for HAT-P-21 b and their residuals for a constant period ($P_{\text{orb}} = 4.12449009 \pm 0.00000090$).

Time of minimum BJD(TDB)–2 400 000	Cycle no.	O – C (day)	Reference
54 996.41312 \pm 0.00069	0	0.000685	Bakos et al. (2011)
55 994.53827 \pm 0.00063	242	–0.000767	CA (this work)
58 902.30440 \pm 0.00108	947	–0.000152	TESS (this work)
58 906.43060 \pm 0.00120	948	0.001558	TESS (this work)
58 910.55289 \pm 0.00093	949	–0.000642	TESS (this work)
58 918.80358 \pm 0.00105	951	0.001067	TESS (this work)
58 922.92610 \pm 0.00115	952	–0.000903	TESS (this work)

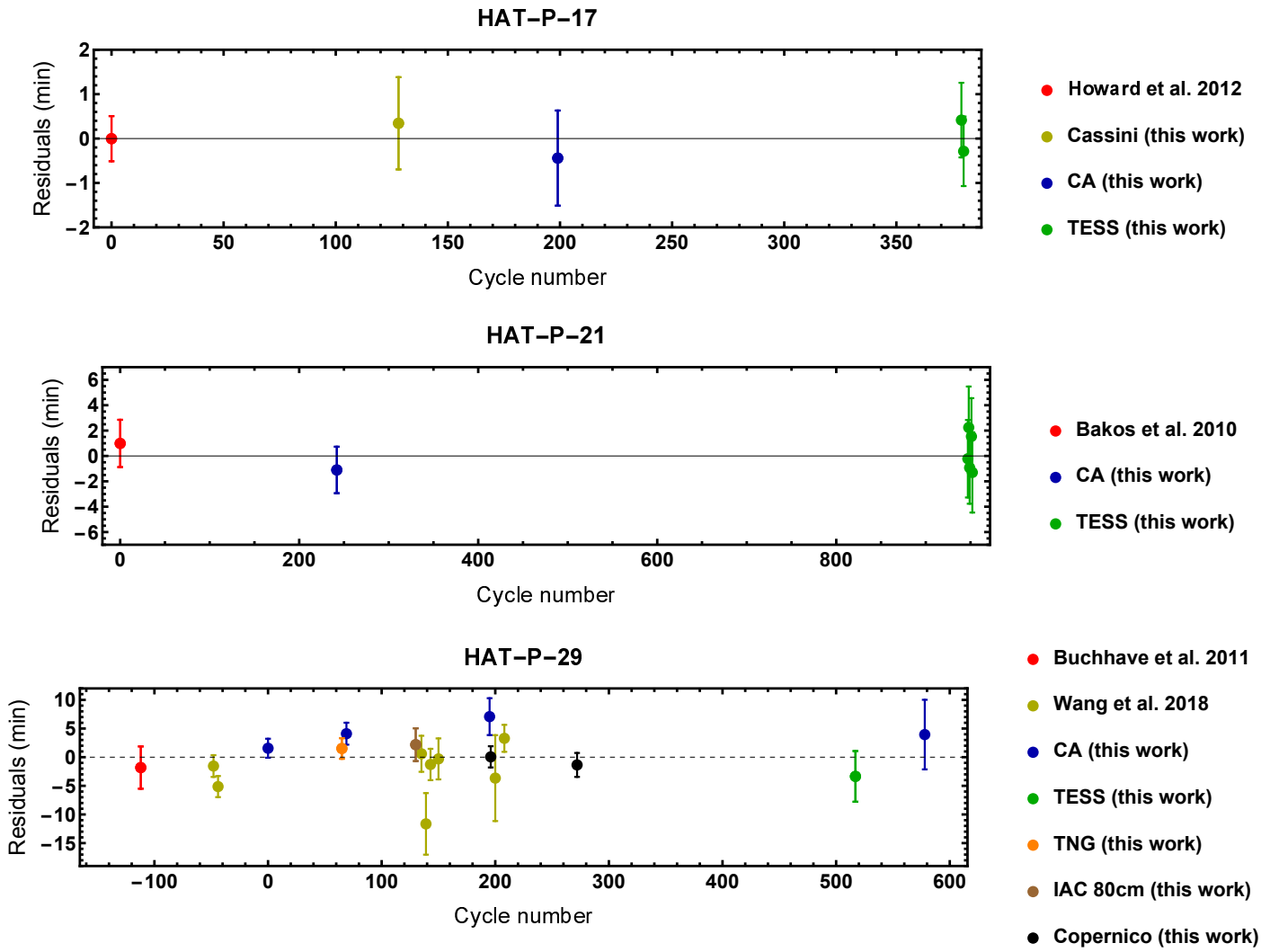


Fig. C.1. Plot of the residuals of the timings of mid-transit of HAT-P-17 b, HAT-P-21 b, and HAT-P-29 b versus a linear ephemeris.

Table C.3. Times of mid-transit for HAT-P-26 b and their residuals for a constant period ($P_{\text{orb}} = 4.23450213 \pm 0.00000076$). With the exception of the last four values, the others were taken from the compilation made by von Essen et al. (2019).

Time of minimum BJD(TDB)–2 400 000	Cycle no.	O – C (day)	Reference
54 860.02786 ± 0.00147	–105.0	–0.00179	Hartman et al. (2011)
55 342.76262 ± 0.00041	9.0	–0.00016	Hartman et al. (2011)
55 304.65218 ± 0.00025	0.0	–0.00009	Stevenson et al. (2016)
56 405.62370 ± 0.00090	260.0	0.00113	Stevenson et al. (2016)
56 545.36220 ± 0.00030	293.0	0.00110	Stevenson et al. (2016)
57 129.72248 ± 0.00017	431.0	0.00022	Stevenson et al. (2016)
57 413.43284 ± 0.00017	498.0	–0.00100	Wakeford et al. (2017)
57 460.01327 ± 0.00016	509.0	–0.00008	Wakeford et al. (2017)
57 510.82710 ± 0.00016	521.0	–0.00026	Wakeford et al. (2017)
57 616.69010 ± 0.00011	546.0	0.00021	Wakeford et al. (2017)
57 112.78503 ± 0.00058	427.0	0.00077	von Essen et al. (2019)
57 125.48930 ± 0.00063	430.0	0.00154	von Essen et al. (2019)
57 129.72283 ± 0.00063	431.0	0.00057	von Essen et al. (2019)
57 163.59738 ± 0.00040	439.0	–0.00089	von Essen et al. (2019)
57 180.53670 ± 0.00057	443.0	0.00042	von Essen et al. (2019)
57 197.47376 ± 0.00046	447.0	–0.00052	von Essen et al. (2019)
57 523.53041 ± 0.00072	524.0	–0.00046	von Essen et al. (2019)
57 887.69984 ± 0.00089	610.0	0.00187	von Essen et al. (2019)
57 904.63796 ± 0.00066	614.0	0.00199	von Essen et al. (2019)
57 921.57698 ± 0.00078	618.0	0.00301	von Essen et al. (2019)
58 226.45772 ± 0.00093	690.0	–0.00034	von Essen et al. (2019)
55 990.64139 ± 0.00078	162.0	–0.00007	CA (this work)
56 765.55640 ± 0.00086	345.0	0.00124	CA (this work)
57 523.53031 ± 0.00055	524.0	–0.00056	CA (this work)
58 175.64477 ± 0.00081	678.0	0.00073	CA (this work)

Table C.4. Times of mid-transit for HAT-P-29 b and their residuals for a constant period ($P_{\text{orb}} = 5.7233746 \pm 0.0000034$).

Time of minimum BJD(TDB)–2 400 000	Cycle no.	O – C (day)	Reference
55 197.57540 ± 0.00181	–112	–0.001260	Buchhave et al. (2011)
55 563.87156 ± 0.00065	–48	–0.001075	Wang et al. (2018)
55 586.76257 ± 0.00061	–44	–0.003564	Wang et al. (2018)
55 838.59570 ± 0.00050	0	0.001084	CA (this work)
56 210.61502 ± 0.00056	65	0.001054	TNG (this work)
56 233.51031 ± 0.00064	69	0.002846	CA (this work)
56 582.63483 ± 0.00120	130	0.001514	IAC 80 cm (this work)
56 611.25060 ± 0.00139	135	0.000411	Wang et al. (2018)
56 634.13560 ± 0.00293	139	–0.008087	Wang et al. (2018)
56 657.03630 ± 0.00109	143	–0.000885	Wang et al. (2018)
56 697.10060 ± 0.00166	150	–0.000208	Wang et al. (2018)
56 954.65758 ± 0.00131	195	0.004915	CA (this work)
56 960.37608 ± 0.00036	196	0.000040	Copernico (this work)
56 983.26700 ± 0.00427	200	–0.002538	Wang et al. (2018)
57 029.05882 ± 0.00068	208	0.002285	Wang et al. (2018)
57 395.35157 ± 0.00033	272	–0.000940	Copernico (this work)
58 797.57696 ± 0.00122	517	–0.002329	TESS (this work)
59 146.70788 ± 0.00217	578	0.002740	CA (this work)

Table D.1. Physical parameters of the planetary system HAT-P-15 derived in this work.

Parameter	Nomen.	Unit	This Work	Source	Kovács et al. (2010)
Stellar parameters					
Spectra class					G5
Effective temperature	T_{eff}	K	5620 ± 20 5620 ± 20	EXOFASTv2 HARPS-N	5568 ± 90
Metallicity	[Fe/H]		$+0.237^{+0.093}_{-0.098}$ $+0.24 \pm 0.10$	EXOFASTv2 HARPS-N	0.22 ± 0.08
Projected rotational velocity ^(a)	$v \sin i_{\star}$	km s^{-1}	1.53 ± 0.25 2.3 ± 0.5	RM fit HARPS-N	2.0 ± 0.5
Convective blue-shift velocity ^(a)	CBV	km s^{-1}	$> -1.73 \pm 0.85$	RM fit	–
Luminosity	L_{\star}	L_{\odot}	$1.072^{+0.100}_{-0.097}$	EXOFASTv2	1.00 ± 0.11
Mass	M_{\star}	M_{\odot}	$1.020^{+0.066}_{-0.060}$	EXOFASTv2	1.013 ± 0.043
Radius	R_{\star}	R_{\odot}	$1.092^{+0.049}_{-0.050}$	EXOFASTv2	1.080 ± 0.039
Mean density	ρ_{\star}	ρ_{\odot}	$1.11^{+0.18}_{-0.15}$	EXOFASTv2	–
Logarithmic surface gravity	$\log g_{\star}$	cgs	$4.371^{+0.047}_{-0.045}$	EXOFASTv2	4.38 ± 0.03
Equal Evolutionary Phase	EEP		389^{+26}_{-42}	EXOFASTv2	–
V-band extinction	A_V	mag	$1.04^{+0.12}_{-0.13}$	EXOFASTv2	–
SED photometry error scaling	σ_{SED}		$7.3^{+2.0}_{-1.3}$	EXOFASTv2	–
Parallax	ϖ	mas	$5.185^{+0.016}_{-0.016}$	EXOFASTv2	–
Distance	d	pc	$192.85^{+0.61}_{-0.60}$	EXOFASTv2	190 ± 8
Age		Gyr	$6.6^{+3.7}_{-3.4}$	EXOFASTv2	$6.8^{+2.5}_{-1.6}$
Orbital parameters					
RV-curve semi-amplitude	K_{\star}	m s^{-1}	–	–	180.6 ± 3.5
Barycentric RV	γ	km s^{-1}	31.7622 ± 0.0009	RM fit	31.7616 ± 0.0014
Projected spin-orbit angle	λ	degree	13 ± 6	RM fit	–

Table D.2. Physical parameters of the planetary system HAT-P-17 derived in this work.

Parameter	Nomen.	Unit	This Work	Source	Howard et al. (2012)	Fulton et al. (2013)
Stellar parameters						
Spectra class					G0	
Effective temperature	T_{eff}	K	5351^{+21}_{-20} 5350 ± 20	EXOFASTv2 HARPS-N	5246 ± 80	–
Metallicity	[Fe/H]		$+0.012^{+0.082}_{-0.080}$ $+0.02 \pm 0.09$	EXOFASTv2 HARPS-N	0.00 ± 0.08	–
Projected rotational velocity ^(a)	$v \sin i_{\star}$	km s ⁻¹	0.84 ± 0.07 0.5 ± 0.5	RM fit HARPS-N	0.3 ± 0.5	0.54 ± 0.15
Convective blue-shift velocity	CBV	km s ⁻¹	-0.46 ± 0.11	RM fit	–	-0.65 ± 0.23
Luminosity	L_{\star}	L_{\odot}	$0.540^{+0.037}_{-0.034}$	EXOFASTv2	0.48 ± 0.04	–
Mass	M_{\star}	M_{\odot}	$0.886 \pm 0.030 \pm 0.024$	ABSDIM	0.857 ± 0.039	–
Radius	R_{\star}	R_{\odot}	$0.860 \pm 0.023 \pm 0.008$	ABSDIM	0.838 ± 0.021	–
Mean density	ρ_{\star}	ρ_{\odot}	1.39 ± 0.12	ABSDIM	–	–
Logarithmic surface gravity	$\log g_{\star}$	cgs	$4.516 \pm 0.027 \pm 0.004$	ABSDIM	4.52 ± 0.02	–
Equal Evolutionary Phase	EEP		348^{+29}_{-26}	EXOFASTv2	–	–
V-band extinction	A_V	mag	$0.250^{+0.089}_{-0.087}$	EXOFASTv2	–	–
SED photometry error scaling	σ_{SED}		$23.0^{+5.6}_{-4.0}$	EXOFASTv2	–	–
Parallax	ϖ	mas	$10.820^{+0.018}_{-0.019}$	EXOFASTv2	–	–
Distance	d	pc	$92.42^{+0.16}_{-0.16}$	EXOFASTv2	90 ± 3	–
Age		Gyr	$6.5^{+3.4+1.6}_{-2.7-2.2}$	ABSDIM	7.8 ± 3.3	–
Transit parameters						
Sum of the fractional radii	$r_p + r_{\star}$		0.0503 ± 0.0015	JKTEBOP	–	–
Ratio of the fractional radii	r_p/r_{\star}		0.1212 ± 0.0012	JKTEBOP	0.1238 ± 0.0010	–
Impact parameter	b		0.27 ± 0.11	JKTEBOP	$0.311^{+0.045}_{-0.067}$	–
Planetary parameters						
Mass	M_p	M_{Jup}	$0.558 \pm 0.015 \pm 0.010$	ABSDIM	0.534 ± 0.018	$0.532^{+0.018}_{-0.017}$
Radius	R_p	R_{Jup}	$1.015 \pm 0.040 \pm 0.009$	ABSDIM	1.010 ± 0.029	–
Mean density	ρ_p	ρ_{Jup}	$0.499 \pm 0.058 \pm 0.004$	ABSDIM	0.518 ± 0.047	–
Surface gravity	g_p	m s ⁻²	13.4 ± 1.0	ABSDIM	12.9 ± 0.6	–
Equilibrium temperature	T_{eq}	K	800 ± 11	ABSDIM	792 ± 15	–
Safronov number	Θ		$0.1105 \pm 0.0046 \pm 0.0010$	ABSDIM	0.109 ± 0.004	–
Orbital parameters						
Reference epoch of mid-transit	T_0	BJD (TDB)	2 454 801.16943 (15)	Timing fit	2 454 801.16943 (20)	–
Period	P_{orb}	days	10.33853781 (60)	Timing fit	10.338523 (9)	–
Inclination	i	degree	89.29 ± 0.30	JKTEBOP	$89.2^{+0.2}_{-0.1}$	–
Semi-major axis	a	au	$0.0892 \pm 0.0010 \pm 0.0008$	ABSDIM	0.0882 ± 0.0014	–
RV-curve semi-amplitude	K_{\star}	m s ⁻¹	–	–	58.8 ± 0.9	$58.58^{+0.69}_{-0.68}$
Barycentric RV	γ	km s ⁻¹	20.3141 ± 0.0021	RM fit	20.13 ± 0.21	20^{+27}_{-16}
Projected spin-orbit angle ^(a)	λ	degree	-27.5 ± 6.7	RM fit	–	19^{+14}_{-16}

Notes. ^(a) Note that Fulton et al. (2013) used a convention with the opposite sign for λ than ours. Therefore, the two results are fully compatible.

Table D.3. Physical parameters of the planetary system HAT-P-21 derived in this work.

Parameter	Nomen.	Unit	This Work	Source	Bakos et al. (2011)
Stellar parameters					
Spectra class					G3
Effective temperature	T_{eff}	K	5699 ± 44 5695 ± 45	EXOFASTv2 HARPS-N	5588 ± 80
Metallicity	[Fe/H]		$+0.046^{+0.085}_{-0.084}$ $+0.04 \pm 0.09$	EXOFASTv2 HARPS-N	0.01 ± 0.08
Projected rotational velocity	$v \sin i_{\star}$	km s^{-1}	3.9 ± 0.9	RM fit	3.5 ± 0.5
Luminosity	L_{\star}	L_{\odot}	$1.52^{+0.11}_{-0.10}$	EXOFASTv2	$1.06^{+0.20}_{-0.16}$
Mass	M_{\star}	M_{\odot}	$0.998 \pm 0.035 \pm 0.020$	ABSDIM	0.947 ± 0.042
Radius	R_{\star}	R_{\odot}	$1.248 \pm 0.049 \pm 0.009$	ABSDIM	1.105 ± 0.083
Mean density	ρ_{\star}	ρ_{\odot}	0.513 ± 0.058	ABSDIM	–
Logarithmic surface gravity	$\log g_{\star}$	cgs	$4.245 \pm 0.033 \pm 0.003$	ABSDIM	4.33 ± 0.06
Equal Evolutionary Phase	EEP		428^{+10}_{-18}	EXOFASTv2	–
V-band extinction	A_V	mag	0.25 ± 0.12	EXOFASTv2	–
SED photometry error scaling	σ_{SED}		$5.6^{+1.5}_{-1.0}$	EXOFASTv2	–
Parallax	ϖ	mas	3.519 ± 0.023	EXOFASTv2	–
Distance	d	pc	284.2 ± 1.8	EXOFASTv2	254 ± 19
Age		Gyr	$7.8^{+2.6+4.4}_{-1.1-2.6}$	ABSDIM	10.2 ± 2.5
Rotational period	P_{rot}	day	15.88 ± 0.02	TFA	–
Transit parameters					
Sum of the fractional radii	$r_p + r_{\star}$		0.1258 ± 0.0064	JKTEBOP	–
Ratio of the fractional radii	r_p/r_{\star}		0.0931 ± 0.0012	JKTEBOP	0.0950 ± 0.0022
Impact parameter	b		0.615 ± 0.056	JKTEBOP	$0.631^{+0.025}_{-0.028}$
Planetary parameters					
Mass	M_p	M_{Jup}	$4.23 \pm 0.15 \pm 0.06$	ABSDIM	4.063 ± 0.161
Radius	R_p	R_{Jup}	$1.130 \pm 0.056 \pm 0.008$	ABSDIM	1.024 ± 0.092
Mean density	ρ_p	ρ_{Jup}	$2.74 \pm 0.40 \pm 0.02$	ABSDIM	$3.77^{+1.28}_{-0.80}$
Surface gravity	g_p	m s^{-2}	82.1 ± 8.1	ABSDIM	95 ± 18
Equilibrium temperature	T_{eq}	K	1367 ± 27	ABSDIM	1283 ± 50
Safronov number	Θ		$0.377 \pm 0.021 \pm 0.003$	ABSDIM	0.413 ± 0.038
Orbital parameters					
Reference epoch of mid-transit	T_0	BJD(TDB)	$2\,454\,996.41243\ (60)$	JKTEBOP	$2\,454\,996.41312\ (69)$
Period	P_{orb}	days	$4.12449009\ (90)$	JKTEBOP	$4.124481\ (07)$
Inclination	i	degree	86.47 ± 0.50	JKTEBOP	87.2 ± 0.7
Semi-major axis	a	au	$0.05037 \pm 0.00058 \pm 0.00034$	ABSDIM	0.0494 ± 0.0007
RV-curve semi-amplitude	K_A	m s^{-1}	–	–	548.3 ± 14.2
Barycentric RV	γ	km s^{-1}	-53.018 ± 0.005	RM fit	-53.190 ± 0.090
Projected spin-orbit angle	λ	degree	-0.7 ± 12.5	RM fit	–

Table D.4. Physical parameters of the planetary system HAT-P-26 derived in this work.

Parameter	Nomen.	Unit	This Work	Source	Hartman et al. (2011)
Stellar parameters					
Spectra class					K1
Effective temperature	T_{eff}	K	5102^{+20}_{-19} 5100 ± 20	EXOFASTv2 HARPS-N	5079 ± 88
Metallicity	[Fe/H]		$+0.005^{+0.091}_{-0.088}$ $+0.05 \pm 0.10$	EXOFASTv2 HARPS-N	-0.04 ± 0.08
Projected rotational velocity	$v \sin i_{\star}$	km s^{-1}	1.9 ± 0.4	HARPS-N	1.8 ± 0.5
Luminosity	L_{\star}	L_{\odot}	$0.357^{+0.021}_{-0.012}$	EXOFASTv2	$0.38^{+0.16}_{-0.06}$
Mass	M_{\star}	M_{\odot}	$0.796 \pm 0.015 \pm 0.026$	ABSDIM	0.816 ± 0.033
Radius	R_{\star}	R_{\odot}	$0.916 \pm 0.062 \pm 0.010$	ABSDIM	$0.788^{+0.098}_{-0.043}$
Mean density	ρ_{\star}	ρ_{\odot}	1.04 ± 0.22	ABSDIM	–
Logarithmic surface gravity	$\log g_{\star}$	cgs	$4.416 \pm 0.063 \pm 0.005$	ABSDIM	4.56 ± 0.06
Equal Evolutionary Phase	EEP		338^{+15}_{-29}	EXOFASTv2	–
V-band extinction	A_V	mag	$0.062^{+0.082}_{-0.044}$	EXOFASTv2	–
SED photometry error scaling	σ_{SED}		$14.8^{+3.9}_{-2.6}$	EXOFASTv2	–
Parallax	ϖ	mas	6.999 ± 0.020	EXOFASTv2	–
Distance	d	pc	$142.88^{+0.42}_{-0.40}$	EXOFASTv2	134^{+18}_{-8}
Age		Gyr	$5.9^{+4.8}_{-3.8}$	EXOFASTv2	10.2 ± 2.5
Transit parameters					
Sum of the fractional radii	$r_p + r_{\star}$		$0.0962312^{+0.0070}_{-0.0068}$	JKTEBOP	–
Ratio of the fractional radii	r_p/r_{\star}		0.0732 ± 0.0011	JKTEBOP	0.0737 ± 0.0012
Impact parameter	b		$0.55^{+0.17}_{-0.13}$	JKTEBOP	$0.30^{+0.11}_{-0.12}$
Planetary parameters					
Mass	M_p	M_{Jup}	$0.0577 \pm 0.0069 \pm 0.0013$	ABSDIM	0.059 ± 0.007
Radius	R_p	R_{Jup}	$0.652 \pm 0.055 \pm 0.007$	ABSDIM	$0.565^{+0.072}_{-0.032}$
Mean density	ρ_p	ρ_{Jup}	$0.195 \pm 0.055 \pm 0.002$	ABSDIM	0.32 ± 0.08
Surface gravity	g_p	m s^{-2}	3.37 ± 0.69	ABSDIM	$4.47^{+0.90}_{-0.92}$
Equilibrium temperature	T_{eq}	K	1080 ± 39	ABSDIM	1001^{+66}_{-37}
Safronov number	Θ		$0.0106 \pm 0.0015 \pm 0.0001$	ABSDIM	0.012 ± 0.002
Orbital parameters					
Reference epoch of mid-transit	T_0	BJD(TDB)	2 455 304.65234 (35)	Timing fit	2 455 304.65122 (35)
Period	P_{orb}	days	4.23450213 (76)	Timing fit	4.234516 (15)
Inclination	i	degree	87.20 ± 0.86	JKTEBOP	$88.6^{+0.5}_{-0.9}$
Semi-major axis	a	au	$0.04748 \pm 0.00030 \pm 0.00052$	ABSDIM	0.0479 ± 0.0006
RV-curve semi-amplitude	K_A	m s^{-1}	–	–	8.5 ± 1.0
Barycentric RV	γ	km s^{-1}	<i>Unconstrained</i>	RM fit	14.72 ± 0.10
Projected spin-orbit angle	λ	degree	<i>Unconstrained</i>	RM fit	–

Table D.5. Physical parameters of the planetary system HAT-P-29 derived in this work.

Parameter	Nomen.	Unit	This Work	Source	Buchhave et al. (2011)
Stellar parameters					
Spectra class					G
Effective temperature	T_{eff}	K	6140^{+29}_{-30} 6140 ± 30	EXOFASTv2 HARPS-N	6087 ± 88
Metallicity	[Fe/H]		$+0.240^{+0.078}_{-0.080}$ $+0.25 \pm 0.08$	EXOFASTv2 HARPS-N	0.21 ± 0.08
Projected rotational velocity	$v \sin i_{\star}$	km s^{-1}	5.2 ± 0.7 4.5 ± 0.8	RM fit HARPS-N	3.9 ± 0.5
Convective blue-shift velocity	CBV	km s^{-1}	> -0.58	RM fit	–
Luminosity	L_{\star}	L_{\odot}	$2.05^{+0.13}_{-0.12}$	EXOFASTv2	$1.84^{+0.47}_{-0.26}$
Mass	M_{\star}	M_{\odot}	$1.206^{+0.048+0.011}_{-0.052-0.016}$	ABSDIM	1.207 ± 0.046
Radius	R_{\star}	R_{\odot}	$1.272^{+0.032+0.004}_{-0.042-0.006}$	ABSDIM	$1.224^{+0.133}_{-0.075}$
Mean density	ρ_{\star}	ρ_{\odot}	$0.586^{+0.049}_{-0.039}$	ABSDIM	–
Logarithmic surface gravity	$\log g_{\star}$	cgs	$4.311^{+0.026+0.001}_{-0.020-0.002}$	ABSDIM	4.34 ± 0.06
Equal Evolutionary Phase	EEP		347^{+41}_{-28}	EXOFASTv2	–
V-band extinction	A_V	mag	0.58 ± 0.11	EXOFASTv2	–
SED photometry error scaling	σ_{SED}		$4.87^{+1.40}_{-0.88}$	EXOFASTv2	–
Parallax	ϖ	mas	$3.135^{+0.020}_{-0.019}$	EXOFASTv2	–
Distance	d	pc	$318.9^{+1.9}_{-2.0}$	EXOFASTv2	322^{+35}_{-21}
Age		Gyr	$2.5^{+1.2+0.4}_{-1.7-0.4}$	ABSDIM	2.2 ± 1.0
Transit parameters					
Sum of the fractional radii	$r_p + r_{\star}$		$0.0964^{+0.0030}_{-0.0020}$	JKTEBOP	–
Ratio of the fractional radii	r_p/r_{\star}		0.08777 ± 0.00063	JKTEBOP	0.0927 ± 0.0028
Impact parameter	b		0.37 ± 0.12	JKTEBOP	$0.591^{+0.062}_{-0.094}$
Planetary parameters					
Mass	M_p	M_{Jup}	$0.773^{+0.050+0.005}_{-0.050-0.007}$	ABSDIM	$0.778^{+0.076}_{-0.040}$
Radius	R_p	R_{Jup}	$1.105^{+0.031+0.003}_{-0.037-0.005}$	ABSDIM	$1.107^{+0.136}_{-0.082}$
Mean density	ρ_p	ρ_{Jup}	$0.536^{+0.056+0.002}_{-0.053-0.002}$	ABSDIM	0.54 ± 0.14
Surface gravity	g_p	m s^{-2}	$15.7^{+1.3}_{-1.2}$	ABSDIM	15.84 ± 2.55
Equilibrium temperature	T_{eq}	K	1281^{+23}_{-26}	ABSDIM	1260^{+64}_{-45}
Safronov number	Θ		$0.0772^{+0.0052+0.0003}_{-0.0050-0.0002}$	ABSDIM	0.077 ± 0.007
Orbital parameters					
Reference epoch of mid-transit	T_0	BJD(TDB)	2 455 838.59462 (65)	Timing fit	2 455 197.5754 (18)
Period	P_{orb}	days	5.7233746 (34)	Timing fit	5.723186 (49)
Inclination	i	degree	88.82 ± 0.50	JKTEBOP	$87.1^{+0.5}_{-0.7}$
Semi-major axis	a	au	$0.06667^{+0.00089+0.00021}_{-0.00096-0.00029}$	ABSDIM	0.0667 ± 0.0008
RV-curve semi-amplitude	K_A	m s^{-1}	–	–	78.3 ± 5.9
Barycentric RV	γ	km s^{-1}	-21.651 ± 0.002	RM fit	-21.670 ± 0.08
Projected spin-orbit angle	λ	degree	-26 ± 16	RM fit	–